

MSX Mid Infrared Imaging of Massive Star Birth Environments. I: Ultracompact H II Regions

Paul A. Crowther^{*}, and Peter S. Conti^{*}

*Department of Physics and Astronomy, University College London, Gower Street, London, WC1E 6BT, UK;
JILA and APS Department, University of Colorado, Boulder CO 80303 USA*

Accepted. Received; in original form

ABSTRACT

We present mid-IR $21\mu\text{m}$ images of a sample of radio selected Ultracompact H II (UCH II) regions, obtained with the Midcourse Space Experiment (MSX). All, with one possible exception, are detected at mid-IR wavelengths, sampling the warm dust emission of the cocoons of the OB star central exciting sources. Many of the UCH II regions have nearby (up to \approx few pc distant) companion dust emission sources, which represent other potential star birth sites. In some objects the companion dominates the IRAS point source catalogue entry for the UCH II region. We compare the mid- and far-IR dust emission, measuring the embedded hot star luminosity, with published UCH II radio emission, measuring the Lyman continuum luminosity. We find a spectral type dependence, as predicted by the standard model of an ultracompact ionized hydrogen region, surrounded by a natal dust shell, with some scatter, which can be understood by consideration of: 1) dust absorption of some fraction of the emitted Lyman continuum photons; 2) fainter companion stars within the UCH II region; 3) the structure of the UCH II regions differing from star to star. Overall, the higher spatial resolution offered by MSX alleviates difficulties often encountered by comparison of IRAS far-IR fluxes with radio derived ionizing fluxes for UCH II regions.

Key words: H II regions; stars: formation; infrared: ISM; stars: early-type

1 INTRODUCTION

Massive O and B-type stars are born individually in molecular clouds or collectively within giant molecular clouds (GMCs), which contain substantial amounts of dust. From the collapse and fractionation of the GMC to the final product of a visible star (or a cluster) a number of physical processes are occurring. These include, but are not limited to, the following stages for the *star*: rapid accretion, the (possible) formation of a disk, slow accretion, the initiation of the zero age main sequence (ZAMS), and normal main sequence evolution. At the same time, but *not* with identical timescales, its surrounding *environment* is evolving: the molecular hydrogen is dissociated then ionized into a gradually expanding H II region; the ice mantles of the dust are evaporated, and the natal cocoon expands, lowering its overall density and opacity. For a recent summary of this general topic, the reader is referred to *The Earliest Stages of Massive Star Birth* (Crowther 2002).

The wavelength at which the material becomes optically thin to the stellar radiation shifts to shorter and shorter

values from the IR. The dust in the cocoon and in the surroundings absorbs and reprocesses the stellar radiation and re-emits it in the far and mid IR (FIR–MIR) regions (from 1 mm down to $10\mu\text{m}$). As this evolution proceeds, we would expect to *observe* the following phenomena for each individual stellar object:

- A ‘Hot Core’ phase (e.g., Kurtz et al. 2000) in which a source of IR dust emission surrounding a buried star is found. The star is sufficiently luminous to heat the dust but it is not (yet?) hot enough to produce sufficient Lyman Continuum photons. Alternatively, the infalling material is “quenching” the formation of an H II region (e.g. Osorio et al. 1999).
- The star forms an ultracompact H II (UCH II) region (e.g., Churchwell 1999ab) which can be identified from its free-free radio emission. The ionized hydrogen is surrounded by a natal dust cocoon which radiates in the FIR–MIR.
- The UCH II region expands, becoming a compact H II (CH II) region, as the dust evaporates and the overlying cocoon expands and thins out (as in, e.g., W49A – Conti & Blum 2002). The FIR–MIR emission gradually diminishes.
- The dust becomes optically thin at visible wavelengths. Eventually the star no longer has any surrounding

^{*} E-mail: pac@star.ucl.ac.uk (PAC) pconti@jila.colorado.edu (PSC)

natal material (e.g., a disk). We will identify this time as the end of the birth process for an individual massive star.

Two key parameters of the birth processes for massive stars are those of the H II region and those of the dust emission. The former can be estimated from the Lyman continuum luminosity, or extreme ultraviolet (EUV) radiation, which is highly dependent on the stellar temperature (e.g. Smith, Norris & Crowther 2002); the latter from the overall stellar luminosity (primarily the UV radiation) along with the dust properties (thickness, extent, and distance from the star). As the birth process goes forward, we would expect both of these parameters to change in response to the stellar evolution and the varying dust in the surrounding cocoon. The dust emission will undergo the largest change as it responds to the evolution of the environment. The Lyman continuum and the UV luminosity should not change dramatically as once the star “turns on” (at the ZAMS) as one would expect that substantial accretion will come to a halt (thus T_{eff} and $L_{\text{bol}} \approx \text{constant}$). For cases in which the central O star is obscured by hundreds of magnitudes of visual extinction, the situation is much simpler at mid-IR wavelengths, where the extinction is several hundred times lower.

Until recently, there had not been any MIR Galactic plane surveys of medium spatial resolution¹. The Midcourse Space Experiment (MSX) remedied this situation, with a complete Galactic plane survey within $|b| \leq 5^\circ$ (Price et al. 2001) at $18''$ spatial resolution. Ultimately, the Space Infrared Telescope Facility (SIRTF) will achieve a much higher spatial resolution. For the moment, however, MSX permits the comparison between radio and MIR fluxes of almost all known massive star birth sites, so as to better understand the relationship between the H II regions and the dust cocoons. In this paper we shall begin with a study of a sample of the UCH II regions in our Galaxy, which are generally believed to be excited by one or a few dominant stars, and ought to represent the simplest cases to investigate. A subsequent paper will consider our results for H II and giant H II (GH II) regions.

We begin in Section 2 by outlining the extraction procedure for obtaining MIR data from the MSX satellite. In Section 3 we list the sample of UCH II objects from the catalogs of Wood & Churchwell (1989) and Kurtz, Churchwell & Wood (1994) that we have studied. We discuss in Section 4 MIR images at $21 \mu\text{m}$ of the UCH II regions, and comment on similarities and differences between the objects. Many objects are multiple, with close (within a few pc) companions. In some of these, the IRAS fluxes of the UCH II regions will have been affected by the nearby objects, in a few cases drastically so. In Section 5 we first consider the relationships among the MSX medium resolution and IRAS low resolution data for our sources. After accounting for the multiplicity of some sources in the IRAS data, and noting a “colour” term in the MSX data, we recover the spectral type dependence of the EUV to UV fluxes of the sources, as predicted by relatively simple models of UCH II regions. Conclusions are given in Section 6.

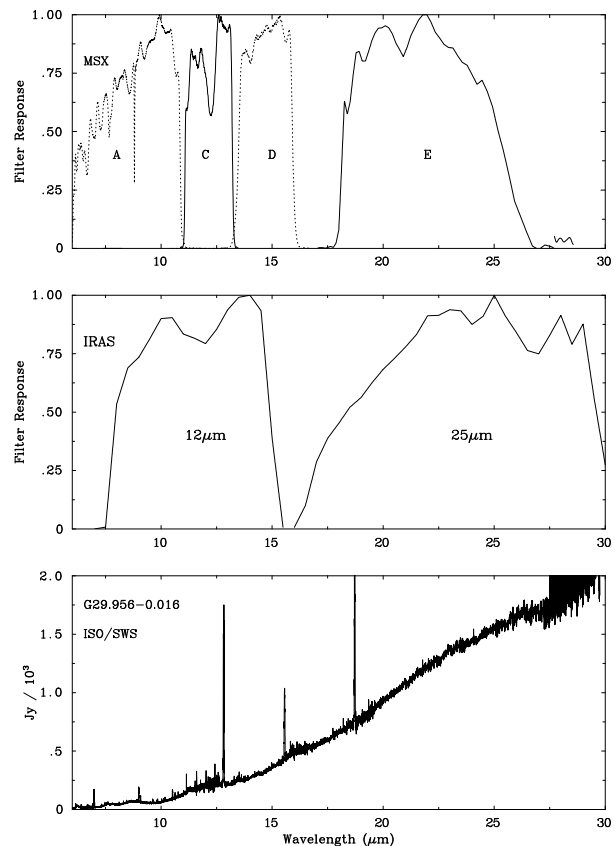


Figure 1. Comparison between the broad band, mid-IR filter profiles of MSX, of which Band C ($12\mu\text{m}$) and Band E ($21\mu\text{m}$) are used here, and the IRAS 12 and $25\mu\text{m}$ filters, together with the ISO/SWS spectrum of the UCH II region G29.956-0.016 (Morisset et al. 2002) for comparison. Strong fine-structure nebulal lines include [Ne II] $12.8\mu\text{m}$, [Ne III] $15.5\mu\text{m}$ and [S III] $18.7\mu\text{m}$.

2 MSX OBSERVATIONS

The U.S. Department of Defense MSX satellite surveyed the entire Galactic plane in four mid-IR spectral bands, named A, C, D, and E, between 6 and $25\mu\text{m}$ at a spatial resolution of $\sim 18.3''$. A description of the telescope and primary instrument, SPIRIT III is given by Price et al. (2001). The entire area within $\pm 4.5^\circ$ of the Galactic plane was surveyed at least twice, with four-fold coverage obtained in the first and fourth quadrants, and to $\pm 3^\circ$ for the remanding quadrants. The redundancy was sufficient to permit combining the datasets onto a uniformly spaced grid, such that the inherent spatial resolution of the instrument was preserved. A total of $1680 \times 95.1' \times 95.1'$ images were created in each of the four mid-IR spectral bands, spaced $90'$ apart in each coordinate, providing $10'$ overlap on adjacent images. Each image provides radiances on a grid in Galactic latitude and longitude, with a grid spacing of $6''$. The image units are of in-band radiance ($\text{W m}^{-2} \text{sr}^{-1}$).

Of the available bands, Band A is the most sensitive, but its filter footprint of $6.8\text{--}10.8\mu\text{m}$ includes the astrophysically strong, broad silicate band at $9.7\mu\text{m}$ and the $8.6\mu\text{m}$ PAH feature. We therefore selected the longer wavelength Band C and Band E observations. These have isophotal central wavelengths of $\lambda_c = 12.13\mu\text{m}$ and $21.34\mu\text{m}$, respectively, with bandwidth of $1.72\mu\text{m}$ and $6.24\mu\text{m}$. MSX Bands C and E are narrower, higher spatial resolution analogues of the well

¹ IRAS had $30'', 30'', 1', 2'$ resolutions for the $12\mu\text{m}$, $25\mu\text{m}$, $60\mu\text{m}$, $100\mu\text{m}$ filters, respectively

Table 1: Mid-IR (MSX/IRAS) and radio (VLA/Arecibo) fluxes (in Jy) for Galactic UCH II regions from Wood & Churchwell (1989, WC) and Kurtz et al. (1994, KCW). UCH II regions with multiple radio peaks are summed together (e.g. G10.47+03 A,B,C).

UCH II G	IRAS	12 μ m MSX	21 μ m MSX	25 μ m IRAS	100 μ m IRAS	2 cm VLA	6 cm VLA	d kpc	Ref	log N Ly C	21 μ m/ 12 μ m ^a	25 μ m/ 21 μ m ^a	21 μ m/ 2 cm ^a	100 μ m 2 cm ^a	Radio morph	MSX morph
[WC89] 5.476–0.243	17559-2420	23	89	194	2170		0.12	14.3	1	48.35	0.59	0.34	—	—	Core-Halo	Extended
[WC89] 5.885–0.392*	17574-2403	128	776	2190	26780	6.54	2.09	2.0	4	48.54	0.78	0.45	2.08	3.61	Shell	Multiple
[WC89] 5.972–1.174	18006-2422	120	762	1842	9036		0.28	2.7	2	47.71	0.80	0.65	—	—	Core-Halo	Extended
[WC89] 8.669–0.356*	18034-2137	<0.8:	10	154	5221	0.57	0.63	4.6	2	48.09	>1.1:	1.19	1.23		Core-Halo	Double
[WC89] 10.304–0.147*	18060-2005	53	189	1042	12010		0.51	6.0	2	48.21	0.55	0.74	—	—	Cometary	Multiple
[WC89] 10.460+0.032*	18056-1952	5.3	18	106	10160		0.12	5.8	2	48.22	0.53	0.77	—	—	Spherical	Double
[WC89] 10.472+0.027*	18056-1952	3.1	19	106	10160		0.05	5.8	2	47.20	0.79	0.75	—	—	Spherical	Double
[WC89] 10.623–0.384*	18075-1956	3.8	41	148	21370	2.13	1.21	17.5	2	49.82	1.03	0.56	1.28		Core-Halo	Multiple
[KCW94] 10.841–2.592	18162-2048	22	149	347	3709	0.009		1.9	3	45.00	0.83	0.37	4.23	5.63		Multiple
[WC89] 11.938–0.616	18110-1854	12	99	222	4930	1.07	0.88	5.2	2	48.28	0.92	0.35	1.96	3.66	Cometary	Double
[WC89] 12.209–0.103*	18097-1825A	2.7	7	10	4221	0.23	0.17	13.5	2	48.62	0.41	0.16	1.46		Cometary	Multiple
[WC89] 12.429–0.049	18099-1811	1.8:	3	8	510		0.04	16.7	1	47.99	0.2:	0.5:	—	—	Cometary	Single
[KCW94] 18.146–0.284	18222-1317	43	138	394	8494	0.011		4.2	3	46.82	0.51	0.45	4.10	5.89		Multiple
[WC89] 19.608–0.234	18248-1158	47	195	407	7093	0.31	0.80	3.5	2	47.62	0.62	0.32	2.80	4.36	Cometary	Extended
[WC89] 20.080–0.135*	18253-1130	4.6	21	76	2761	0.51	0.38	3.4	2	47.78	0.66	0.56	1.61	3.73	Shell	Double
[WC89] 23.455–0.201*	18319-0834	<1.2:	2:	122	9595		0.01	9.0	1	46.84	0.2::	1.8:	—	—	Spherical	Multiple
[WC89] 23.711+0.171*	18311-0809	20	78	184	2904		0.15	8.9	2	48.02	0.59	0.37	—	—	Core-Halo	Double
[WC89] 25.716+0.049*	18353-0628	5.0	31	105	2435		0.02	9.3	2	47.08	0.79	0.53	—	—	Spherical	Multiple
[KCW94] 28.200–0.049	18403-0417	21	70	178	3937	0.77		9.1	3	48.47	0.53	0.40	1.96	3.71		Single
[KCW94] 28.288–0.364	18416-0420	63	473	821	4358	0.94		3.3	3	47.81	0.88	0.24	2.70	3.66		Multiple
[WC89] 29.956–0.016	18434-0242	208	1022	1697	11670	2.66	1.37	7.4	2	49.17	0.69	0.22	2.58	3.64	Cometary	Multiple
[WC89] 30.535+0.021	18443-0210	13	47	88	1067	0.46	0.45	13.8	1	48.96	0.56	0.27	2.01	3.37	Cometary	Single
[WC89] 31.414+0.310	18449-0115	2.0	15	52	2815	0.48	0.38	7.9	2	48.49	0.87	0.52	1.51	3.76	Core-Halo	Single
[KCW94] 32.798+0.190	18479-0005	30	123	298	5473	0.45		13.0	3	48.87	0.61	0.38	2.44	4.08		Single
[WC89] 33.915+0.110	18502+0051	30	137	250	2429	0.36	0.50	8.2	1	48.54	0.66	0.26	2.44	3.68	Core-Halo	Extended
[WC89] 34.255+0.145	18507+0110	106	434	1106	32460	4.18	1.58	4.0	2	48.83	0.61	0.41	2.02	3.89	Cometary	Multiple
[WC89] 35.199–1.743	18592+0108	88	471	1073	13960	2.37	1.93	3.1	2	48.40	0.73	0.34	2.30		Cometary	Extended
[WC89] 37.545–0.112	18577+0358	13	48	106	1867		0.23	9.9	2	48.30	0.57	0.34	—	—	Core-Halo	Extended
[KCW94] 37.874–0.399	18593+0408	42	129	304	4524	3.07		9.2	3	49.18	0.49	0.37	1.62	3.18		Single
[WC89] 43.889–0.783	19120+0917	15	74	145	1511	0.51	0.36	4.2	2	47.96	0.69	0.29	2.16	3.47	Cometary	Extended

(1) Wood & Churchwell (1989); (2) Churchwell et al. (1990); (3) Kurtz et al. (1994); (4) Acord et al. (1998)

(a) entries are presented in logarithms for ready comparison with figures.

Table 1: (continued)

	UCH II G	IRAS	12 μ m MSX	21 μ m MSX	25 μ m IRAS	100 μ m IRAS	2 cm VLA	6 cm VLA	d kpc	Ref	log N Ly C	21 μ m/ 12 μ m ^a	25 μ m/ 21 μ m ^a	21 μ m/ 2 cm ^a	100 μ m 2 cm ^a	Radio morph	MSX morph
[WC89]	45.071+0.132	19110+1045	47	234	494	7497	0.59	0.14	6.0	2	48.33	0.70	0.32	2.60	4.10	Spherical	Single
[WC89]	45.122+0.132	19111+1048	260	1007	1395	7497	3.68	1.17	6.9	2	49.25	0.59	0.14	2.44	3.31	Cometary	Multiple
[WC89]	45.456+0.060	19120+1103	71	367	640	7890		0.42	6.6	2	48.21	0.71	0.24	—	—	Cometary	Multiple
[WC89]	45.466+0.046*	19120+1103	0.6	17	640	7890		0.08	6.0	2		1.46	1.6:	—	—		Multiple
[KCW94]	48.606+0.024*	19181+1349	9.3	33	175	5227	0.06		9.7	3	47.59	0.55	0.72	2.74			Multiple
[WC89]	49.490–0.370*	19213+1424	402	1658	4344	26760	5.35	0.50	6.6	2	49.37	0.62	0.42	2.49		Cometary	Multiple
[WC89]	54.094–0.060	19294+1836	6.7	22	50	2136		0.002	7.9	1	46.00	0.52	0.36	—	—	Spherical	Double
[KCW94]	60.884–0.128	19442+2427	30	208	425	5174	0.029		2.3	3	46.50	0.84	0.31	3.86	5.26		Double
[WC89]	61.473+0.093	19446+2505	64	458	1185	13210		0.25	6.5	2	47.22	0.85	0.41	—	—	Spherical	Extended
[KCW94]	70.293+1.600*	19598+3324	290	927	1780	12980	5.15		8.6	3	49.29	0.51	0.28	2.26	3.38		Multiple
[KCW94]	70.330+1.586*	19598+3324	15	58	1780	12980	0.23		8.0	3	48.15	0.60	1.49	2.41			Multiple
[WC89]	75.783+0.343*	20198+3716	8.2	45	480	6985		0.04	4.1	2	46.78	0.74	1.03	—	—	Cometary	Double
[WC89]	75.835+0.400	20197+3722	109	656	1225	6985		0.27	5.5	1	47.86	0.78	0.27	—	—	Core-Halo	Double
[KCW94]	76.383–0.621	20255+3712	164	1050	2510	13130	0.017		1.0	3	45.06	0.81	0.38	4.80	5.90	Spherical	Extended
[KCW94]	78.438+2.659	20178+4046	26	339	551	2877	0.036		3.3	3	46.83	1.12	0.21	3.98	4.91		Single
[KCW94]	81.679+0.537	...	27	307			0.88		2.0	3	47.52	1.06	—	2.54	—	Core-Halo	Double
[KCW94]	81.683+0.541	...	33	397			0.61		2.0	3	47.35	1.08	—	2.81	—	Core-Halo	Double
[KCW94]	109.871+2.113	20543+6145	5.3	249	820	20470	0.027		0.7	3	44.62	1.67	0.52	3.97	5.88	Multiple	Double
[KCW94]	111.282–0.663	23138+5945	16	92	233	2164	0.080		2.5	3	46.68	0.75	0.40	3.06	4.43	Core-Halo	Multiple
[KCW94]	111.612+0.374	23133+6050	38	371	581	2694	0.68		5.2	3	48.21	0.98	0.19	2.74	3.59	Shell	Single
[KCW94]	133.947+1.064	02232+6137	32	250	536	10600	2.53		3.0	3	47.92	0.89	0.33	2.00	3.62	Spherical	Single
[KCW94]	139.909+0.197	03035+5819	25	237	396	1297	0.018		4.2	3	46.43	0.98	0.22	4.11	4.85	Spherical	Single
[KCW94]	192.584–0.041*	06099+1800	<1.5:	16	371	5285	0.026		2.5	3	46.03	>1.05	1.37	2.79			Multiple

(1) Wood & Churchwell (1989); (2) Churchwell et al. (1990); (3) Kurtz et al. (1994); (4) Acord et al. (1998)

(a) entries are presented in logarithms for ready comparison with figures.

known IRAS $12\mu\text{m}$ and $25\mu\text{m}$ bands as illustrated in Fig. 1, where ISO/SWS spectroscopy of the prototypical UCH II region G29.956–0.016 is also presented (Morisset et al. 2002). The calibration and photometric accuracy of MSX are discussed in detail by Egan et al. (1999). The zero magnitude flux is based on the Kurucz model for Vega (Cohen et al. 1992), and correspond to $9.259 \times 10^{-13} \text{ W m}^{-2}$ (Band C) and $3.555 \times 10^{-13} \text{ W m}^{-2}$ (Band E).

Individual UCH II images were obtained from the MSX Image Server at IPAC <http://irsa.ipac.caltech.edu/applications/MSX/>. For our purposes, we sought integrated MIR fluxes in Janskys for comparison with radio fluxes. Consequently, the MSX point source catalogue was not appropriate, given the need to use apertures precisely centred on the radio coordinates. Spatial integration was measured in GAIA (Draper, Gray & Berry 2001) using a circular aperture of radius 3 pixel ($18''$). Aperture centres were selected to precisely mimic those of the corresponding radio observations. Thin annuli, with 3 pixel radii ($18''$), were used to correct for the background flux levels, taking care to avoid sources in the annuli. Spatial integration over the images provides fluxes in units of W m^{-2} , after correction for the $6'' \times 6''$ pixel-area, i.e. $8.4615 \times 10^{-10} \text{ sr}$. Division by the filter bandwidth then provides fluxes in $\text{W m}^{-2} \text{ Hz}^{-1}$ ($= 10^{26} \text{ Jy}$). Finally, a multiplication by 1.113 is required to convert the square area pixels into the correct Gaussian area (Cohen, priv. comm.). The total scale factor for Band C corresponds to a multiplicative factor of 27.45 in order to convert the IPAC integrated fluxes to mJy, whilst the corresponding factor is 23.72 for Band E.

3 SELECTION OF SAMPLE

We included all the UCH II regions from Wood & Churchwell (1989) and Kurtz et al. (1994) for which 2 or 6 cm radio fluxes (and so ionizing fluxes) exist, and contain MSX datasets for which data could be extracted. We have omitted G15.042–0.676 since its MIR flux is totally dominated by the surrounding GH II region M17. Distances have been kinematically determined from Galactic rotation model by Churchwell, Walmsley & Cesaroni (1990) or Kurtz et al. (1994), except where noted. Table 1 lists the parameters of the UCH II regions we have studied in the MIR. The various columns will be discussed in due course.

4 MID-IR MORPHOLOGIES

4.1 Discussion of individual objects

Figures A.1– 8 in the Appendix contain $21\mu\text{m}$ images of our sources at spatial scales of $10' \times 10'$, having first been transformed from (l, b) to (RA, Dec.) for epoch J2000.0. We have indicated the physical scales, using the distances derived from Churchwell et al. (1990) or Kurtz et al. (1994).

We have also made corresponding images of the $12\mu\text{m}$ data from MSX (not presented here). For the most part, these appear similar with the exception that 1) several UCH II sources are not visible at this wavelength and 2) some other point sources are seen at the shorter wavelength but not the longer one. The former are inordinately red sources

with a cool dust origin, whilst the latter are probably stars, which would typically be brighter at $12\mu\text{m}$. NIR images of the central $0.5' \times 0.5'$ for many UCH II regions are presented by Hanson, Luhman & Rieke (2002).

To facilitate the presentations below, we have indicated with an asterisk (*) those sources for which the lower resolution IRAS photometry and its Point Source Catalog (PSC) will be affected by a brighter nearby companion as suggested by our images.

4.1.1 [WC89] G5.476–0.243

The $21\mu\text{m}$ image of G5.476 is presented in Fig. A1(a), revealing a single core, but within a spatially extended source. The nearest mid-IR source is much fainter, and is probably unrelated as it lies $150''$ (at least $\sim 10 \text{ pc}$) away to the north east.

4.1.2 [WC89] G5.885–0.392*

G5.885, alias W28 A2(1), is amongst the brightest UCH II of our sample at mid-IR wavelengths. The mid-IR morphology is shown in Fig. A1(b), and reveals an elongation to the SE, probably due to another source. From MSX, a separate spatially extended region is only $2.5'$ away ($\sim 1.5 \text{ pc}$) which also contains a bright point source at G5.898–0.441 (same IRAS source as G5.885). Kim & Koo (2001) have recently presented 21cm VLA observations with a spatial resolution comparable to MSX, revealing a morphology very similar to Fig. A1, with G5.885 corresponding to their more compact western source. Since the larger eastern source is a radio emitter it is not a hot core. These are embedded within a large region ($14 \times 9'$) of weak emission.

Note that we have adopted 2kpc for the distance to G5.89 as determined by Acord, Churchwell & Wood (1998). This object was used as the basis of the standard model of an UCH II region by Wolfire & Churchwell (1994). Feldt et al. (1999) discuss arcsecond resolution NIR and MIR images of G5.885.

4.1.3 [WC89] G5.972–0.174

G5.972, within the Lagoon Nebula (M8), appears as an extended mid-IR source in the MSX image Fig. A1(c), although it is uniquely surrounded by a very large, extended halo, several parsec in extent. The flux enclosed within a radius of 36 arcsec is a factor of 2 times larger than the nominal (18 arcsec radius) value. Stecklum et al. (1998) discuss high spatial resolution optical, IR and radio observations of G5.972. 21cm data, showing the larger scale structure, are presented by Kim & Koo (2001), revealing a very large ($14' \times 10'$) extended envelope surrounding the UCH II region, including an arclike structure originating from the SE, that has no obvious mid-IR counterpart.

4.1.4 [WC89] G8.669–0.356*

From our sample, G8.669 has amongst the reddest $12\text{--}21\mu\text{m}$ index, such that it is barely detectable at $12\mu\text{m}$, with a corresponding low dust temperature. The mid-IR flux measured

by IRAS at the location of G8.669–0.356 is actually dominated by a probable hot core some $40''$ or 0.9 pc away - Fig. A1(d). Consequently, previously derived luminosities obtained from the IRAS PSC for this UCH II represent a strong overestimate, i.e. 19 Jy was measured by IRAS at $12\mu\text{m}$ versus <0.8 Jy obtained here for the UCH II region.

4.1.5 [WC89] G10.304–0.147*

The mid-IR image of G10.304, within the W31 H II complex, is shown in Fig. A1(e), and reveals it to be spatially extended, with a faint dust tail extending north-west, with a probably related strong extended source, centred $70''$ away (~ 2 pc) to the NE at G10.321–0.157. IRAS 18060–2005 contains both IR sources, such that the IR luminosity of G10.304 has previously been strongly overestimated. Kim & Koo (2001) present 21cm VLA observations of G10.304, also revealing strong, concentrated emission in the bright mid-IR source to the NE. A faint radio envelope surrounds both components, extending $13' \times 5'$ to the NW and SE.

4.1.6 [WC89] G10.472+0.032* and 10.460+0.027*

From Fig. A1(f) MSX separates the two UCH II regions G10.46 and G10.47 $45''$ or 1.2 pc apart, hitherto unresolved by IRAS (18056–1952). A third mid-IR source lies to the south, alias IRAS 18056–1954. Hatchell et al. (2000) present JCMT SCUBA images of this region, revealing a strong peak in the $850\mu\text{m}$ flux at the source A of Wood & Churchwell (1989), with G10.460+0.027A also weakly detected. Garay et al. (1993) show 20cm radio observations.

4.1.7 [WC89] G10.623–0.384*

MSX images of the environment of G10.623 reveal a complex of mid-IR sources, as shown in Fig. A2(a), of which the UCH II itself has a nearby, fainter, point source $25''$ to the north east, plus a brighter mid-IR source G10.598–0.383 to the south west $90''$ (8 pc) away. The IRAS source 18075–1956 is dominated by the latter, at least in the 12 – $25\mu\text{m}$ bands.

4.1.8 [KCW94] G10.841–2.592

Fig. A2(b) shows that a bright IR source is coincident with the radio position of G10.841, with two close, fainter companions $\sim 30''$ away to the east and north-west. G10.841 itself, coincident with the GGD 27 complex, has been the subject of high resolution mid-IR imaging by Stecklum et al. (1997). Peeters et al. (2002) have recently presented ISO spectroscopy of G10.841.

4.1.9 [WC89] G11.938–0.616

Fig. A2(c) indicates that G11.938 is elongated, with a much fainter IR source $70''$ away (1.4 pc) to the SW.

4.1.10 [WC89] G12.209–0.103*

The UCH II G12.209 is a very weak mid-IR source according to Fig. A2(d), with two potentially related and much brighter IR sources that dominate the $21\mu\text{m}$ flux. The closest of these is $60''$ or 4 pc away to the SW at G12.193–0.104. Kim & Koo (2001) present low resolution 21cm VLA observations of G12.209, revealing a spatial morphology very similar to the mid-IR, with the two sources to the SW and SE brighter than the UCH II itself, such that these are not hot cores. Faint extended radio emission also extends NE of the G12.209, as in the mid-IR. Hatchell et al. (2000) present $850\mu\text{m}$ and $450\mu\text{m}$ SCUBA images of this region, showing a peak associated with the UCH II region.

4.1.11 [WC89] G12.429–0.049

G12.429 appears single but is extremely weak at $12\mu\text{m}$ and $21\mu\text{m}$ as measured by MSX. It has the bluest color index of our sample, implying the highest dust temperature. This object is well isolated with no other mid-IR source within 10 pc as illustrated in Fig. A2(e). Kim & Koo (2001) have presented 21cm radio data of G12.429.

4.1.12 [KCW94] G18.146–0.284

Fig. A2(f) reveals that G18.146 lies at the peak of a very extended (~ 2 pc) region of dust emission with multiple sources arranged along a NS axis.

4.1.13 [WC89] G19.608–0.234

G19.608 is spatially extended with a faint halo, according to Fig. A3(a), albeit no other nearby mid-IR companions.

4.1.14 [WC89] G20.080–0.135*

MSX images reveal G20.080 to be double, with a potentially related companion only $36''$ or 0.6 parsec to the south – see Fig. A3(b). The companion is brighter than G20.080 at $12\mu\text{m}$, though comparable at $21\mu\text{m}$, such that it may be stellar in origin. IRAS 18253–1130 contains both sources. Faint, nearby companions lie to the north and west.

4.1.15 [WC89] G23.455–0.201*

This UCH II is unique amongst our sample in that it is essentially invisible to MSX at *both* 12 and $21\mu\text{m}$ – Fig. A3(c). The strong IRAS source 18319–0834 commonly used to constrain the spectral energy distribution of G23.455 is in fact located $80''$ to the south, within a complex, extended region centred at G23.437–0.209. Consequently, we measure an upper limit of ~ 2 Jy for G23.46 itself at $21\mu\text{m}$, in contrast with 122 Jy obtained from the IRAS PSC at $25\mu\text{m}$. We could find no evidence for an error in the published radio position, or with our MSX coordinates. Indeed, Kim & Koo (2001) present 21cm radio observations that confirm the mid-IR view, namely that G23.455 lies at the northern edge of a strong radio source, spatially coincident with G23.437–0.209 which must be more evolved than a hot core. Further to the south radio emission extends along an east-west direction, coincident with a series of fainter mid-IR sources.

4.1.16 [WC89] G23.711+0.171*

Fig. A3(d) reveals that G23.711 is double, with a companion $36''$ to the south east. The companion has a comparable $12\mu\text{m}$ flux to the UCH II, but is 30% fainter at $21\mu\text{m}$ which suggests that it may be stellar in origin. IRAS 18311–0809 contains both sources. Kim & Koo (2001) included G23.711 in their 21cm survey of UCH II regions, also showing a spatial extension from G23.711 to the SE.

4.1.17 [WC89] G25.716+0.049*

The UCH II region G25.716 appears to be single, albeit with a nearby brighter mid-IR region $100''$ or 4 pc to the south – see Fig. A3(e). IRAS 18353–0628 is centred on the brighter IR source, such that an IR luminosity inferred from IRAS for the UCH II would represent a strong overestimate. This UCH II region was also studied at 21cm by Kim & Koo (2001). Although the radio spatial morphology closely matches the mid-IR view, Kim & Koo argued that the source to the south is not physically connected to G25.716 owing to a very different radial velocity.

4.1.18 [KCW94] G28.200–0.049

G28.200 appears to be single from MSX $21\mu\text{m}$ images presented in Fig. A3(f).

4.1.19 [KCW94] G28.288–0.364

MSX imaging reveals the core of G28.288 be elongated, as illustrated in Fig. A4(a). There is also a companion a factor of four times fainter at $21\mu\text{m}$ $100''$ to the east. IRAS 18416–0420 contains both sources.

4.1.20 [WC89] G29.956–0.016

G29.956 is the prototypical cometary UCH II region, and is amongst the brightest of our sample at mid-IR wavelengths despite its large distance (7.4 kpc, Churchwell et al. 1990). Fig. A4(b) reveals the core of G29.956 to be extended. Very high spatial resolution ($0.5''$) mid-IR imaging has recently been presented by De Buizer et al. (2002). The closest mid-IR source is G29.935–0.055, an extended region located $2.5'$ away to the south east, which is also prominent in 21cm radio observations of Kim & Koo (2001). These, together with a further source to the SW, lie within a complex extended radio region.

This UCH II region is excited by an O5–6V star according to near-IR spectra discussed by Watson & Hanson (1997) and Hanson et al. (2002). Peeters et al. (2002) present the ISO spectrum of G29.956, which is analysed by Morisset et al. (2002) with reference to the ionizing source (see, however, Lumsden et al. 2003).

4.1.21 [WC89] G30.535+0.021

G30.535 appears to have a single core in the mid-IR as shown in Fig. A4(c), albeit with a faint halo.

4.1.22 [WC89] G31.414+0.310

G31.414 appears to have a single core, again with an extended halo – see Fig. A4(d). Garay et al. (1993) present 2-20cm radio images of G31.414. The SCUBA sub-mm emission reveals a central peak coincident with the UCH II region, with some extension to the south (Hatchell et al. 2000).

4.1.23 [KCW94] G32.798+0.190

G32.798 is single according to our MSX images presented in Fig. A4(e). Peeters et al. (2002) presented the ISO spectrum of G32.80. Garay et al. (1993) present 2-20cm VLA radio observations, whilst Kurtz et al. (1999) have identified extended emission from 3.6cm imaging.

4.1.24 [WC89] G33.915+0.110

G33.915 again appears to have a single core, but with a faint halo – Fig. A4(f). The ISO spectrum of G33.92+0.11 is presented by Peeters et al. (2002). Fey et al. (1992) and Garay et al. (1993) discuss the radio morphology of G33.915 from 2 to 20cm.

4.1.25 [WC89] G34.255+0.145

G34.255 appears fuzzy with a strong dust tail extending east-west below the central source – Fig A5(a). G32.455 is a well studied cometary UCH II region at radio wavelengths (e.g. Fey et al. 1992).

4.1.26 [WC89] G35.199–1.743

G35.199 contains a central dense, core but with an envelope with a condensation extending $90''$ or ≈ 2 pc to the south – see Fig. A5(b). Takahashi et al. (2000) infer stellar properties of G35.199 from mid-IR imaging in the [Ne II] $12.8\mu\text{m}$ filter.

4.1.27 [WC89] G37.545–0.112

G37.545 appears spatially extended with another possible embedded source – Fig. A5(c). Kim & Koo (2001) present 21cm radio observations of G37.545.

4.1.28 [KCW94] G37.874–0.399

G37.87 appears to be single, with faint extended dust emission extending $\sim 60''$, as illustrated in Fig. A5(d).

4.1.29 [WC89] G43.889–0.783

This UCH II appears as a point source at $21\mu\text{m}$ according to Fig. A5(e), with extended emission extending SE containing a condensation. The sub-mm SCUBA image of Hatchell et al. (2000) reveals a single peak towards to the radio position.

4.1.30 [WC89] G45.071+0.132 and G45.122+0.132

G45.071 and G45.122 are 3' apart on the sky, such that their physical separation is ~ 6 pc if they lie at a common distance of 6.5 kpc. Churchwell et al. (1990) suggest a distance of 6 kpc to G45.07 and 6.9 kpc to G45.12. These UCH II regions have previously been resolved by IRAS at 12 and $25\mu\text{m}$, such that G45.071 is IRAS 19110+1045, whilst G45.122 is IRAS 19111+1048. The latter has a companion $50''$ away to the north west, at G45.134+0.144 – see Fig. A5(f). This weakly contaminates the $25\mu\text{m}$ IRAS measurement of G45.122. Lumsden et al. (2003) infer a cluster of OB stars, rather than a single O star, power both UCH II regions, while Takahashi et al. (2000) infer stellar properties of G45.122 from mid-IR imaging in [Ne II] $12.8\mu\text{m}$. Hunter et al. (1997) discuss sub-mm observations of the molecular cores containing these two UCH II regions, suggesting that G45.122+0.132 is at a more advanced state of star formation.

*4.1.31 [WC89] G45.456+0.060 and G45.466+0.046**

G45.456 is very bright at mid-IR wavelengths, with an elongated core. Of the three nearby, much fainter $21\mu\text{m}$ sources seen in Fig. A6(a), only the object $60''$ to the north west is also seen at $12\mu\text{m}$. Indeed, the faint source $70''$ to the east of G45.456 is the UCH II G45.466+0.046 which has an exceptionally red mid-IR color of $F(21\mu\text{m}/12\mu\text{m}) > 30$. If these lie at the same distance their separation is 2 pc. A further bright source lies $4.5'$ away to the NW at G45.479+0.133. Another H II region, which is very bright at $21\mu\text{m}$, lies to the NW at G45.479+0.133, and is also thought to be part of the same star forming complex.

Feldt et al. (1998) discuss high spatial resolution near- and mid-IR observations of G45.456, whilst Garay et al. (1993) present 6 and 20 cm radio maps. Lumsden et al. (2003) have recently argued in favour of a cluster of OB stars ionizing the UCH II region, instead of a single star.

*4.1.32 [KCW94] G48.606+0.024**

This UCH II region is revealed as a point source within a large extended mid-IR emitting region, with a nearby bright source centred on G48.595+0.044 – see Fig. A6(b). The IRAS source 19181+1349 is dominated by the latter object. Another faint source lies nearby to the north. 3.6 cm imaging by Kurtz et al. (1999) revealed extended emission in the H II region surrounding G48.606.

4.1.33 [WC89] G49.490–0.370 (W51d)*

This is an extremely complicated portion of the well known GH II region W51 at mid-IR wavelengths, as indicated by Fig. A6(c). G49.490 is an exceptionally bright source at $21\mu\text{m}$. Another mid-IR bright source lies very close, $40''$ (≈ 2 pc) away, to the south east at G49.488–0.381, that possesses a bright dust tail. IRAS 19213+1424 includes both these bright sources, such that the IR luminosity of the UCH II region will be strongly overestimated via use of the IRAS flux. Consequently for this particular example, arguments made by Lumsden et al. (2003) in favour of a *cluster* of OB stars powering this UCH II region will be affected. Several

other fainter mid-IR sources lie to the south, south west, west and north east. High resolution mid-IR imaging and spectroscopy of W51d, alias W51 IRS2, have been presented by Okamoto et al. (2001) and by Kraemer et al. (2001).

4.1.34 [WC89] G54.094–0.060

This is an isolated double source, with a dust tail extending to the south east – see Fig. A6(d).

4.1.35 [KCW94] G60.884–0.128

This source, alias Sh 2-87, sits within an small extended region with a nearby (1 pc if physically related) point source to the west at G60.872–0.107 – see Fig. A6(e). Peeters et al. (2002) present the ISO spectrum of G60.884. Kurtz et al. (1999) identified extended radio emission at 3.6 cm in G60.884.

4.1.36 [WC89] G61.473+0.093

G61.473 (Sh 2-88) appears to have an spatially extended core, plus an extensive dust halo with a diameter of $80''$ (~ 2 pc) – see Fig. A6(f). 6 cm and 20 cm radio observations have been presented by Garay et al. (1993).

4.1.37 [KCW89] G70.293+1.600 and G70.330+1.586**

Fig. A7(a) reveals that G70.293, alias K3-50A, lies at the centre of a small cluster of at least three sources, of which it is the brightest mid-IR source. G70.330 is much fainter and lies $2.5'$ away to the NE. All sources contribute to the IRAS source 19598+3324.

Okamoto et al. (2003) have recently presented mid-IR spectroscopy and imaging of G70.293 suggesting that it is ionized by a cluster of two or three late O stars, instead of a single dominant source. Lumsden et al. (2003) arrives at similar conclusions from near-IR observations.

*4.1.38 [WC89] G75.783+0.343**

The relatively high spatial resolution obtained by MSX permits the UCH II G75.783 to be identified as a rather weak mid-IR source, in contrast to the commonly assumed coincidence between G75.78 and IRAS 20198+3716 – see Fig. A7(b). The IRAS flux, at least for the 12– $25\mu\text{m}$ bands, is totally dominated by a source $60''$, or 1.2 pc to the south west. The IRAS source has a $12\mu\text{m}$ flux of 423 Jy of which only 8 Jy is from G75.78 3 according to our Band C MSX images.

4.1.39 [WC89] G75.835+0.400

G75.835 (Sh 2-105), located 5 arcmin north of G75.783 is a bright mid-IR source, dominating IRAS 19111+1048. It has a close, much fainter companion $45''$ to the north – see Fig. A7(c). If these lie at the same distance, as would appear probable, this corresponds to a separation of 1.2 pc. Garay et al. (1993) present 2–20 cm radio maps of G75.835.

4.1.40 [KCW89] G76.383-0.621

This UCH II, alias Sh 2-106, appears to be single, though is spatially extended some $90''$ in the north-south direction. A faint IR point source is seen $80''$ (≈ 0.4 pc) to the south in Fig. A7(d). Kurtz et al. (1999) identified extended radio emission in G76.383.

4.1.41 [KCW94] G78.438+2.659

Fig. A7(e) indicates that G78.438 appears single, with a very faint dust tail to the south, and no nearby mid-IR source. Once again, Kurtz et al. (1999) observed extended radio emission at 3.6 cm for G78.438.

4.1.42 [KCW94] G81.679+0.537 and G81.683+0.541 (DR21)

Mid-IR imaging of DR21 reveals a $21\mu\text{m}$ bright extended source, containing G81.679+0.537 and G81.683+0.541, though centred on neither. In addition, a diffuse region extends east-west – see Fig. A7(f). Several faint point sources are also seen, the brightest of which is $3'$ to the NW. Kraemer et al. (2001) present high resolution mid-IR imaging of DR21, revealing separate N and SW components at $13\mu\text{m}$, together with comparisons to radio continuum measurements. No IRAS source is catalogued at the position of DR21. Peeters et al. (2002) present a mid-IR spectrum obtained with ISO.

4.1.43 [KCW94] G109.871+2.113

G109.871 is a bright, though extended, $21\mu\text{m}$ source, as shown in Fig. A8(a), with a faint companion $2'$ (≈ 1 pc) north west. G109.871 is extremely faint at $12\mu\text{m}$ such that it has a $21/12\mu\text{m}$ ratio of ~ 47 , the highest of our present sample of UCH II regions, indicating the lowest dust temperature. Unusually, no extended radio emission was observed by Kurtz et al. (1999).

4.1.44 [KCW94] G111.282-0.663

Fig. A8(b) reveals G111.282 (Sh 2-157B) to lie at the centre of an extended $2'$ complex, with faint emission to the NE. In addition, a companion lies several arcmin to the south at G111.279-0.707 that is extremely red, since it is barely detectable at $12\mu\text{m}$. No stellar photospheric features were detected by Hanson et al. (2002) from NIR spectroscopy of G111.282. Kurtz et al. (1999) identified extended radio emission surrounding this UCH II region.

4.1.45 [KCW94] G111.612+0.374

G111.61, alias Sh 2-157, is identified as a bright, spatially extended source with no nearby mid-IR companions in Fig. A8(c). Hanson et al. (2002) present NIR spectroscopy of the central source, revealing strong nebular He I $2.11\mu\text{m}$ emission, indicating a very hot (early O) ionizing source. Peeters et al. (2002) discuss the ISO spectrum of G111.612. No extended radio emission was observed in this UCH II region by Kurtz et al. (1999).

4.1.46 [KCW94] G133.947+1.064

This UCH II region, alias W3(OH), appears single at mid-IR wavelengths – see Fig. A8(d) – with a halo and a nearby faint companion $\sim 30''$ to the east. High resolution mid-IR imaging was presented recently by Stecklum et al. (2002).

4.1.47 [KCW94] G139.909+0.197

G139.909 appears to be a point source at $21\mu\text{m}$, Fig. A8(e), but has a close faint $12\mu\text{m}$ companion, which is probably a star. Hanson et al. (2002) present NIR spectroscopy of (probably) the central star of G139.909, revealing a late O or early B spectral type.

4.1.48 [KCW94] G192.584-0.041*

This UCH II region is extremely faint at $21\mu\text{m}$ relative to a nearby extended source, $1'$ to the south which dominates the IRAS 12 and $25\mu\text{m}$ fluxes – see Fig. A8(f). Indeed, G192.584 is not detected with MSX at $12\mu\text{m}$, such that it has a $21/12\mu\text{m}$ flux ratio in excess of >11 . Other faint, equally red, sources lie to the south and to the west which are probably other members of the same complex.

4.2 Overall morphology

We have listed in Table 1 the UCH II radio morphology² as found by the radio measurements at spatial scales of a few arcsec. We also indicate in this table our evaluation of the dust morphology as indicated by the MSX $21\mu\text{m}$ images, which is on spatial scales of a few arcmin or more. We call sources *single* if the core image appears roughly circular with little or no elongation. Those labelled *extended* are elongated or have fainter dust surrounding the core which may contain other objects. Sources with multiple cores, or with “companions” nearby are called *double*, or *multiple*. There does not seem to be any correlation between the radio and the dust morphologies, which may not be too surprising given the very different scales of these phenomena.

Many of the sources appear to be resolved by MSX, i.e. their diameters are $\geq 18''$, the spatial resolution of the instrument. This resolution corresponds to different physical scales, depending on the source distances, as may be seen by examination of Figures A1–8. Looking at the two nearest sources, their core diameters correspond to a few tenths of a pc. Many others have larger core diameters of up to ≈ 1 pc. The surrounding halos extend to even greater distances in some cases.

We were surprised to find most of our MSX images to have MIR sources in addition to the UCH II region located nearby. Those we consider double or multiple have companions within about 5 pc (projected) if they are at the same distance (radial velocities are generally not available). In some cases, already noted in the discussion of individual objects, the IRAS photometry will be dominated by the companion. At $21\mu\text{m}$ normal stars will be fainter than at $12\mu\text{m}$, so we expect the companions to be dust emission sources.

² Radio morphologies are listed as either cometary, core-halo, spherical or shell by Wood & Churchwell (1989)

Some might be ‘hot cores’ (e.g., Churchwell 2002), although Kim & Koo (2001) revealed that many such companions are radio sources, indicating that they are at a more advanced state of evolution. There are 53 sources in our Table 1, of which 12 are single with no extended dust or obvious companions. It appears that in most cases, this sample of *field UCH II objects are not isolated star formation sites but are connected with nearby (few pc distant) activity.*

5 COMPARISON BETWEEN MIR–FIR AND RADIO FLUXES

5.1 The standard model

A well known model of the dust emission from an UCH II region (e.g., Churchwell 1999) is spherically symmetric (1D) with two major constituents: the inner ionized hydrogen volume and an outer thick shell of molecular gas and dust. The outer boundary of the ionized hydrogen region is typically up to 0.1 pc in radius, the surrounding cocoon dust some ten times larger. The cocoon is optically thick to the visible–UV radiation of the exciting star and is thus heated by it (Kahn 1974; Osorio et al. 1999).

The dust emission will dominate the observed spectral energy distribution (SED). This typically has a broad peak, close to $100\mu\text{m}$, fortuitously coincident with the long wavelength IRAS filter. Thermal radiation from the dust cocoon extends from about 1 mm down to a few microns. This dust is *not* at a single temperature but has a broader wavelength distribution than a black body. Most of the dust is at a temperature of about 30K, although some of that nearest the star could be at 100K or more (see discussion in Wolfire & Churchwell 1994). Their modelling of the IRAS SEDs indicated that the dust density distribution in the shell was more or less constant (no fall off with radius). A more recent study by Hatchell et al. (2000) using the DUSTY radiative transfer code required a $r^{-3/2}$ density profile distribution to reproduce the sub-mm radial emission profiles. 2D geometries in the near future will provide a better model for comparison purposes. We use the phrase ‘standard model’ to refer to the situation where the radio emission comes from an inner spherical region and the IR emission from the outer cocoon.

Radiation from wavelengths longer than about 1 mm will arise from the inner region of ionized hydrogen surrounding the central OB star. Lyman continuum photons are emitted from the stellar surface and ionize the hydrogen. According to the standard model, the H II region is *ionization* bounded, that is, all the LyC photons are used up within this volume which produces the radio emission. Note that some photons emitted by the star might be absorbed by dust within the H II region³. These photons would not produce radio emission and would not be counted when one is trying to infer properties of the star from the H II region. Whether this is an important problem for UCH II regions will be discussed below.

We are interested here in the relationship between the

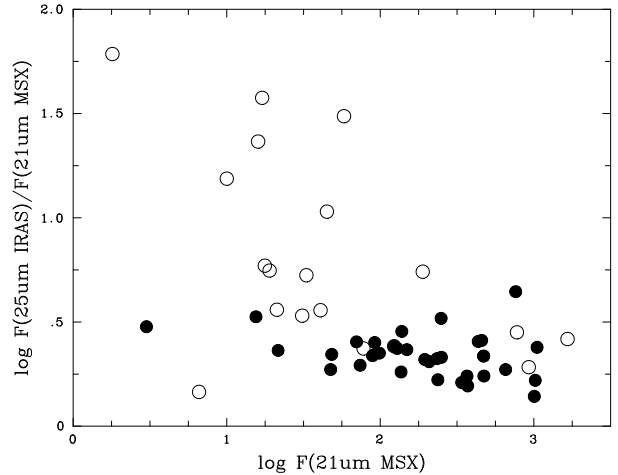


Figure 2. Comparison between $30''$ aperture $25\mu\text{m}$ IRAS fluxes for Galactic UCH II regions and the $18''$ aperture $21\mu\text{m}$ MSX fluxes, based on data from Wood & Churchwell (1989) and Kurtz et al. (1994). Open circles: sources with brighter close companions; filled circles: sources without such companions. Agreement between the $21\mu\text{m}$ and $25\mu\text{m}$ measurements for sources without companions is good.

IR emission from the dust, which is determined by the stellar luminosity which for hot stars is the UV radiation, and the radio emission of the H II region, which is dependent upon the EUV luminosity of the star. This ratio ought to be spectral type dependent, ranging from 10^3 for early O type stars to 10^6 for early B types (Churchwell 1999). We will now see if the standard model of UCH II regions can fit stars with this wide a range of parameters.

5.2 Comparison of MSX $21\mu\text{m}$ flux with $25\mu\text{m}$ IRAS flux

We have identified a number of UCH II regions which at the spatial resolution of MSX are found to have nearby companions. These may be affecting the IRAS Point Source Catalog (PSC) entries, particularly the long wavelength $100\mu\text{m}$ filter with its $2'$ spatial resolution. In some cases the companion may dominate the flux, even at the shorter wavelengths. As we wish to infer the parameters of the dust cocoons from the MIR–FIR photometry, let us first examine quantitatively how much of a problem contamination plays.

In Figure 2 we plot the $25\mu\text{m}/21\mu\text{m}$ (log) flux ratio vs. the $21\mu\text{m}$ (log) flux (both are distance independent), where we have distinguished between sources without bright companions and those with them. Many of the latter have wildly different fluxes in the MSX and IRAS filters. Leaving these outliers aside, there is no trend of flux ratio with the strength of the MIR flux, and the mean ratio (not log units) is 2.20 ± 0.46 . The differences in the IRAS and MSX filter bandwidth alone accounts for a factor of 1.6 (recall Fig. 1). The rest is due to the IRAS filter being somewhat redwards of the MSX filter, thus nominally brighter in these red sources. In the following figures we shall concentrate on those objects without bright companions (filled circles) although we will show all sources throughout.

³ Lyman α photons are efficiently absorbed by dust in compact H II regions and probably represents the dominant dust heating mechanism

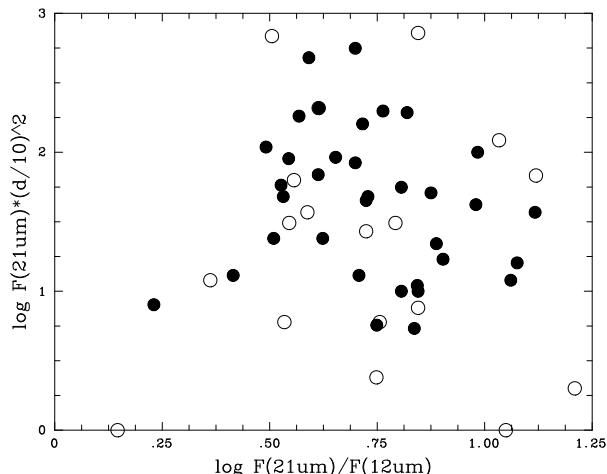


Figure 3. IR colour-magnitude diagram of UCH II regions: Comparison between MIR colour ($21\mu\text{m}/12\mu\text{m}$) and $21\mu\text{m}$ flux scaled to a uniform distance of 10 kpc. As above, we distinguish between those sources with bright companions and those without. In this figure there is essentially no distinction.

One further note of caution is that for our comparison between MSX and radio fluxes, we have limited the mid-IR flux to the spatial resolution of the instrument, such that the total mid-IR flux of extended sources is underestimated. One outlier in Fig. 2 without a close companion, G5.972–1.174, is highly extended, such that our quoted MSX $21\mu\text{m}$ flux of 762 Jy, increases dramatically for larger apertures, i.e. 1600 Jy (36 arcsec radius) or 2400 Jy (60 arcsec radius). Consequently, the quoted $25\mu\text{m}/21\mu\text{m}$ flux of 2.4 is highly aperture sensitive for this one case especially, decreasing to 1.15 with an adopted 36 arcsec radius, or 0.77 for a one arcminute MSX radius.

5.3 Color-magnitude diagrams

Stellar astrophysicists typically prepare colour magnitude diagrams (CMD), which plot the luminosities of stars vs. their colors, or temperature. As we are not observing the exciting stars of the UCH II regions directly, we have to use other measurable parameters. The MIR–FIR fluxes, corrected to a uniform 10 kpc distance, may serve as a surrogate for the luminosity since nearly all of the stellar radiation has been converted to heating the dust cocoon. We can measure the color of the cocoon, an indicator of the dust temperature distribution, by obtaining the MSX $21\mu\text{m}/12\mu\text{m}$ flux ratio.

Fig. 3 presents an MIR CMD, namely the MSX $21/12\mu\text{m}$ index versus the $21\mu\text{m}$ flux, adjusted to a uniform distance of 10 kpc. We see a fairly wide scatter along the abscissa suggesting a large range of colours for the dust cocoons. This indicates that they do not all have the same slopes of the SED on the short wavelength side. The vertical extent, of course, represents different luminosities of the dust, thus of the central exciting stars. We see that there is little if any dependence of the luminosity (ordinate) on the color. Thus the dust luminosity and its SED are not correlated. The color of the dust cocoon will have to be accounted for in detailed modeling of individual sources.

We have considered whether effects other than temperature might affect the $21/12\mu\text{m}$ index, namely nebular contributions and extinction. Many sources are strong emitters in mid-IR fine structure lines of neon and sulphur, of which [Ne II] $12.8\mu\text{m}$ and [S III] $18.7\mu\text{m}$ lie in the 12 and $21\mu\text{m}$ filters. From inspection of a range of UCH II regions observed with ISO/SWS (e.g. G29.956–0.016 in Fig. 1), we conclude that this contribution at most 10% of the continuum dust emission. Variable extinction may be more problematic, since many sources are very heavily reddened. The $12\mu\text{m}$ Band C filter of MSX does include the red wing of the familiar silicate absorption feature centred at $9.7\mu\text{m}$ (e.g. Fig 2 of Morris et al. 2000), this is compensated to some extent by the much greater linewidth of the $21\mu\text{m}$ Band E filter. Nevertheless, one should bear in mind that $21\mu\text{m}$ and especially $12\mu\text{m}$ flux measurements are affected to some degree by extinction, in contrast with far-IR and radio fluxes.

5.4 MIR vs. radio relationships

Radio fluxes from Wood & Churchwell (1989) and Kurtz et al. (1994) were generally obtained at high spatial resolution with interferometric techniques, and so are restricted to the central regions of each UCH II region at $0.5\text{--}5''$ resolution. In contrast, the somewhat lower spatial resolution of the MSX fluxes presented here sample a larger region. There is increasing evidence in the literature that some LyC photons are finding their way out beyond the UCH II region where they ionize the hydrogen found there.

These halos have been investigated by Kurtz et al. (1999) and Kim & Koo (2001) who re-examined the radio properties of UCH II regions at larger scales (see also Araya et al. 2002). As we have discussed above, there is an excellent consistency between the Kim & Koo 21cm dataset and our mid-IR MSX images, particularly for complex regions such as G5.885–0.392, G10.304–0.147, G12.209–0.103 and G23.455–0.201. In most cases, the larger aperture leads to a higher radio flux, i.e. the commonly adopted radio fluxes (dense, ionized components) provide only a fraction of the total when the less dense, extended surrounding regions are considered. These extended regions range in size from $15''$ to more typically $60''$. Larger aperture fluxes generally exceed the Wood & Churchwell (1989) and Kurtz et al. (1994) VLA results at 6cm by a factor of 3, although the factor may be as large as 29 (for G60.88–0.13; Araya et al. 2002).

Unfortunately, the sample observed with these techniques is small to date, so we have to follow the original VLA fluxes from Table 1 for our analysis of the UCH II region sample. Nevertheless, we will keep this multiplicative factor in mind in what follows, hoping that it is reasonably the same from source to source. The existence of ionized hydrogen halos of UCH II regions implies that the standard model is *density*, not *ionization*, bounded.

We ratio the $21\mu\text{m}$ and VLA B-array 2cm fluxes as a function of the observed N(LyC) photons in Fig. 4 for all UCH II regions for which 2cm fluxes are available. The abscissa, which is distant dependent, is used as a surrogate for the temperature (spectral type) of the exciting star. We see a trend in the MIR/radio flux ratio with the temperature of the exciting star, which is predicted by the standard model. A linear regression analysis leads to

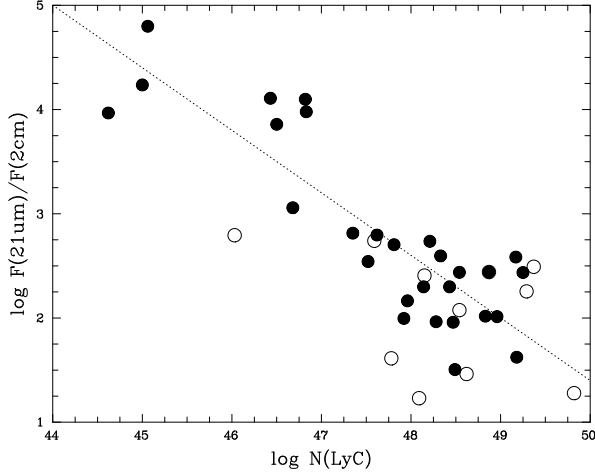


Figure 4. Comparison between the MIR/radio ($21\mu\text{m}/\text{VLA } 2\text{cm}$) index of Galactic UCH II regions versus ionizing fluxes, again discriminating between sources with bright companions (open circles) and those without (filled circles). A linear fit to the latter is shown as a dotted line (see text).

$$\log(21\mu\text{m}/2\text{cm}) = C_1(50 - \log N(\text{LyC})) + C_2,$$

where $C_1 = 0.600 \pm 0.068$ and $C_2 = 1.401 \pm 0.178$. This is an empirical relationship which will be useful below for its scatter. A slight note of caution is necessary, however, since the $21\mu\text{m}/2\text{cm}$ ratio would be suppressed in the case of extremely high extinction, because the denominator has no dependence, whilst the numerator has a weak dependence – recall that a visual extinction of 100 magnitudes corresponds to a $21\mu\text{m}$ extinction of 0.5 mag (0.2 dex in Fig. 4).

Kurtz et al. (1994) made an analogous plot of IR to radio flux ratio but used the $100\mu\text{m}$ luminosity rather than the N(LyC) photons. They attributed their scatter to two sources: 1) some LyC photons are being absorbed by the dust and 2) some UCH II regions have multiple sources within them. Either or both of these effects could contribute to our scatter in the following ways: 1) If LyC photons are being absorbed by the dust, a point in Fig. 4 would have moved leftwards and upwards in the diagram; 2) If other stars are present and contributing to the IR flux, a point would have moved vertically upwards. Before attributing our scatter to these same influences we realized that here might be an additional parameter influencing the scatter in our plot.

The $21\mu\text{m}$ wavelength has a strong color term (recall Fig. 3) due to it being on the short wavelength slope of the SED, which is itself not uniform from object to object. We will next show an analogous plot using the IRAS $100\mu\text{m}$ flux, which is at the peak of the dust cocoon SED, taking account of the problem of the multiplicity of the sources.

5.5 FIR vs. radio relationships

In Fig. 5 we plot the IRAS $100\mu\text{m}$ flux/VLA B-array 2 cm flux vs. the N(LyC) photons. We see a very clear linear relationship, extending over 5 orders of magnitude in the number of N(LyC) photons and 3 orders in the IR/radio ratio. A fit to the UCH II regions without bright companions is

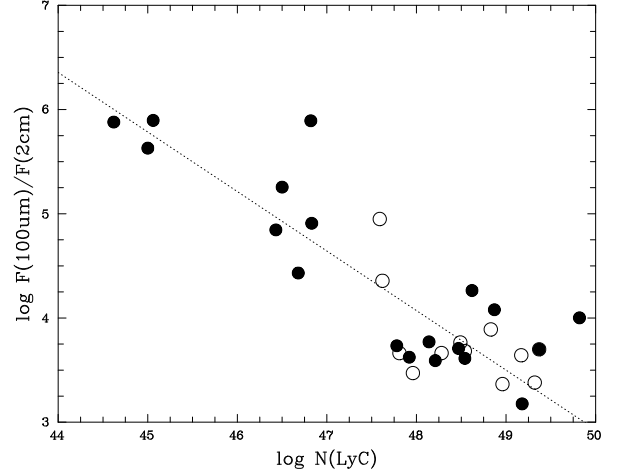


Figure 5. Comparison between FIR /radio (IRAS $100\mu\text{m}$ /VLA 2cm) index of Galactic UCH II regions versus ionizing fluxes, for sources with bright companions (open circles) and those without (filled circles). A linear fit to the latter is shown as a dotted line (see text).

shown as a dotted line in Fig. 5. The empirical regression relation is

$$\log(100\mu\text{m}/2\text{cm}) = C_3(50 - \log N(\text{LyC})) + C_4,$$

where $C_3 = 0.571 \pm 0.048$ and $C_4 = 2.929 \pm 0.124$, having omitted the one outlier, G18.15–0.28, which lies well above the mean relation. (This source sits in a very extended region of dust emission with multiple fainter sources which may be affecting its fluxes – see Fig. A2). Notice that the scatter here is significantly less than that shown in Fig. 4, when we used the $21\mu\text{m}$ wavelength. The scatter in this diagram presumably represents the effects of dust absorption of LyC photons and that of other stellar contributors to the dust emission. These effects are relatively small.

Since many Wood & Churchwell (1989) UCH II sources were without 2cm flux measurements, in Fig. 6 we compare the IRAS $100\mu\text{m}$ to VLA 6cm index with Lyman continuum ionizing flux. This relationship is similar to that shown in the previous figure, except that there are no fainter stars in the Wood & Churchwell sample. Arrows indicate revised locations for those UCH II observed (or inferred) with larger radio beams (Araya et al. 2002). Notice that these more or less move *along* the empirical relationship towards higher radio fluxes and N(LyC), in keeping with predictions.

Finally, let us construct a CMD for the exciting central stars of UCH II regions, using as the ordinate the FIR luminosity, and as abscissa, the N(LyC) photons as a surrogate for the spectral type. This result is shown in Figure 7, and we reversed the abscissa so it looks like those of stellar astrophysicists. Considering only the stars unaffected by companions, we see that there is a range in luminosity of 5 magnitudes between early O stars N(LyC) photons with $\approx 10^{49.5} \text{ s}^{-1}$ and early B stars, with N(LyC) photons $\approx 10^{45} \text{ s}^{-1}$. This is broadly in agreement with models of hot, luminous stars as indicated in the key in the Figure. This follows the recent OB grid of Smith et al. (2002), adapted to take effect of the revised temperature calibration of Martins, Schaerer

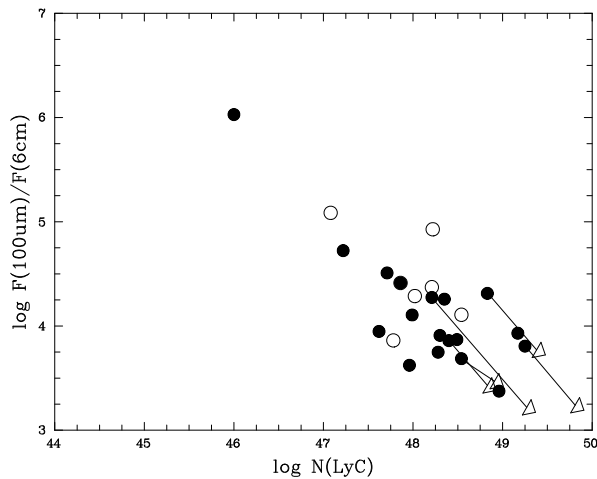


Figure 6. Comparison between FIR /radio (IRAS 100 μ m /VLA 6cm) index of Galactic UCH II regions versus ionizing fluxes, from Wood & Churchwell (1989) with symbols as before. Arrows indicate revised 6cm and ionizing fluxes using larger aperture Arecibo observations (Araya et al. 2002).

& Hillier (2002). We have not converted the FIR luminosity to a magnitude system on the figure, since the 100 μ m flux does not take into account dust emission from longer wavelengths. This correction is a factor of a few. Similarly, the N(LyC) photons measured for the inner UCH II region have not accounted for the halo of ionized material. We already saw that this correction was also a factor of a few.

We see in Figure 7 that the objects without much influence of a companion have a reasonably tight relationship between their luminosities and temperatures. We can interpret this diagram as the ZAMS for hot, luminous stars. There is not much scatter although G18.15–0.28 (recall Figure 5) again stands out above the relation. It could be that this UCH II region has several close companions which contribute to the luminosity of the dust, but not to the N(LyC) photons.

6 CONCLUSIONS

Young, massive stars are obscured at UV, optical and near-IR wavelengths due to extremely high extinction from their circumstellar, birth envelopes. For every magnitude of extinction suffered in the mid-IR at 25 μ m, that in the K-band is 20 times greater, whilst the visual extinction is 200 times greater (e.g. Fig 2 of Morris et al. 2000). Consequently, only 10% of OB stars ionizing an UCH II region can be detected in the near-IR (Hanson et al. 2002). Since the star may not be directly observed in most cases, we have to rely on indirect probes at mid-IR, far-IR and radio wavelengths. In the current study we have presented MSX mid-IR observations of dust surrounding UCH II regions. These are sites of massive star birth, with central ionizing stars spanning spectral types of early B in G109.871+2.113 to early O in G10.623–0.384, at a higher spatial resolution than that which IRAS offered. Only 25% of all radio selected UCH II regions surveyed here were *not* found to be extended, or have close companions, themselves often radio emitters. In most cases, field UCH II

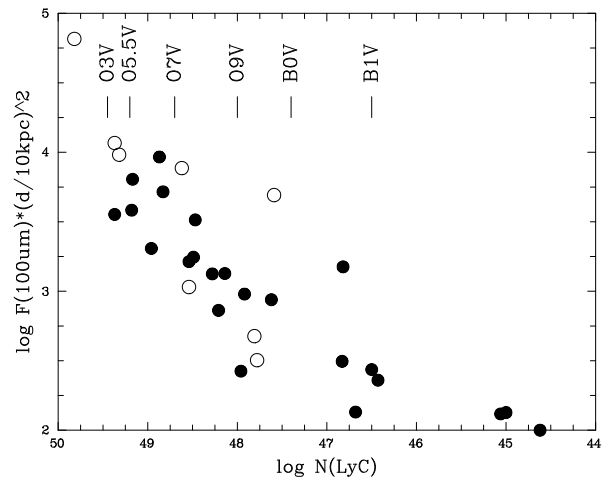


Figure 7. Comparison between Lyman continuum flux inferred from radio and IRAS 100 μ m flux scaled to a uniform distance of 10 kpc. Again, we distinguish between those sources with (open) and without (filled) bright companions. We can interpret this diagram as the ZAMS for hot, luminous stars, and so indicate typical ionizing fluxes for OB dwarfs (adapted from Smith et al. 2002, following the revised dwarf temperature scale of Martins et al. 2002).

regions lie within larger complexes of star formation. Consequently, previous use of IRAS fluxes for the spectral energy distributions of UCH II regions would have led to strong overestimates of bolometric luminosities in $\sim 50\%$ of cases. This result, although widely anticipated, reduces inferred stellar luminosities, *without* affecting LyC fluxes. This may affect recent claims that clusters of stars, rather than a single dominant source, ionize individual UCH II regions (e.g. G49.490–0.370, Lumsden et al. 2003).

Comparison between MSX 21 μ m and 12 μ m fluxes permit colour information on the dust cocoon to be made in each case. We find a large range of colours, indicating a variety of dust temperature distributions. Consequently, because of this colour term, we may not blindly use 21 μ m fluxes as representative of the dominant far-IR luminosity, and so resort to the IRAS 100 μ m fluxes for those UCH II regions that appear to well isolated. From a comparison between MSX 21 μ m and IRAS 25 μ m fluxes, we identify those IRAS sources for which the UCH II regions are the sole or principal source of mid-IR radiation, and so the likely principal source of far-IR flux. A comparison is made between the 100 μ m flux and Lyman continuum radiation, inferred from radio observations, revealing a linear relationship, as predicted by the standard model for UCH II regions. Any remaining scatter may be attributed to dust absorption by the emitted LyC radiation and fainter companions within the UCH II region. Finally, we compare the UCH II region Lyman continuum flux with observed 100 μ m fluxes, adjusted to a uniform distance, again revealing a tight spectral type dependence, also in general accord with the standard model.

Overall our results are encouraging, but we should not neglect remaining problems. As discussed above, MSX reveals large scale information on the stellar nurseries of massive stars, with a spatial resolution somewhat higher than

IRAS. In contrast, ground-based near-IR and mid-IR observations at a much better spatial resolution reveal structure on a quite different, complementary scale. Most radio observations compare more closely with the latter, except for recent data of Kurtz et al. (1999) and Kim & Koo (2001). In the future, 2MASS and SIRTf will permit comparisons of large numbers of UCH II regions to be made on a similar scale. Individual massive Young Stellar Objects (YSOs) have recently been studied using MSX by Lumsden et al. (2002). In contrast, our next study will investigate the mid-IR properties of a complete radio sample of Giant H II (GH II) regions in the Milky Way.

ACKNOWLEDGEMENTS

PAC and PSC appreciate continuing support by the Royal Society and the NSF, respectively. We wish to thank Martin Cohen for help with MSX flux calibration, Robert Stencel, Nathan Smith and Matt Redman for useful comments. This research made use of data products from the Midcourse Space Experiment. Processing of the data was funded by the Ballistic Missile Defense Organization with additional support from NASA Office of Space Science. This research has made use of the NASA/IPAC Infrared Science Archive, which is operated by the Jet Propulsion Laboratory, California Institute of Technology, under contract with the National Aeronautics and Space Administration, and the SIMBAD database, operated at CDS, Strasbourg, France. GAIA is a Starlink derivative of the ESO Skycat catalogue and image display tool.

REFERENCES

- Acord, J.M., Churchwell E., Wood D.O.S., 1998, *ApJ* 495, L107
 Araya E., Hofner P., Churchwell E., Kurtz S., 2002, *ApJS* 138, 63
 Churchwell E., 1999a, *ARA&A* 40, 27
 Churchwell, E. 1999b, in *The Origins of Stars and Planetary Systems*, ed. C.J. Lada & N.D. Kylafis (Dordrecht: Kluwer), p515
 Churchwell E., 2002, in *Hot Star Workshop III: The Earliest Stages of Massive Star Birth* (ed. P.A. Crowther), ASP Conf. Ser 267, 3
 Churchwell, E., Walmsley, C.M., & Cesaroni, R. 1990, *A&A Supp.* 83, 119
 Cohen, M., Walker R.G., Barlow, M.J., Deacon J.R., 1992, *AJ*, 104, 1650
 Conti, P.S. & Blum, R.D. 2002, in *Hot Star Workshop III: The Earliest Stages of Massive Star Birth* (ed. P.A. Crowther), ASP Conf. Ser 267, 297
 Crowther P.A. (ed.), 2002, *Hot Star Workshop III: The Earliest Stages of Massive Star Birth*, ASP Conf. Ser 267
 De Buizer J.M., Watson A.M., Radomski J.T., Pina R.K., Telesco C.M., 2002, *ApJ* 564, L101
 Draper, P.W., Gray N., & Berry, D.S., 2001, *Starlink User Note* 214.9, Rutherford Appleton Laboratory, UK
 Egan M.P., et al. 1999, *MSX Point Source Catalog Explanatory Guide*, AFRL-VS-TR-1999-1522, (Springfield: NTIS)
 Feldt M., Stecklum, B., Henning Th., et al., 1998, *A&A* 339, 759
 Feldt M., Stecklum, B., Henning Th., Launhardt R., Hayward T.L., 1999, *A&A* 346, 243
 Fey A.L., Claussen M.J., Gaume R.A., Nedouha G.E., Johnston K.J., 1992, *AJ* 103, 234
 Garay G., Rodriguez L.F., Moran J.F., Churchwell E., 1993, *ApJ* 418, 368
 Hatchell J., Fuller G.A., Millar T.J., Thompson M.A., Macdonald, G.H., 2000, *A&A* 357, 637
 Hanson M.M., Luhman, K.L., Rieke G.H., 2002, *ApJS* 138, 35
 Hunter T.R., Phillips T.G., Menten, K.M., 1997, *ApJ* 478, 283
 Kahn F.D., 1974, *A&A* 37, 149
 Kim K-T, Koo B-C, 2001, *ApJ* 549, 979
 Kraemer K.E., Jackson J.M., Deutsch L.K. et al. 2001, *ApJ* 561, 282
 Kurtz, S.E., Churchwell, E., & Wood, D.O.S. 1994, *ApJS*, 91, 659
 Kurtz S.E., Watson A.M., Hofner P., Otte, B., 1999, *ApJ* 514, 232
 Kurtz, S.E., Cesaroni, R., Churchwell, E., Hofner, P., & Walmsley, C.M. 2000 in *Protostars and Planets IV*, ed. V. Mannings, A.P.Boss, & S.S. Russell (Tucson: Univ. of Arizona Press), p299
 Lumsden S.L., S.L., Hoare M.G., Oudmaier R.D., Richards D., 2002, *MNRAS* 336, 621
 Lumsden, S.L., Puxley P.J., Hoare M.G., Moore T.J.T., Ridge, N.A., 2003, *MNRAS* in press (astro-ph/0212135)
 Martins F., Schaerer D., Hillier D.J., 2002, *A&A* 382, 999
 Morris P.M., van der Hucht K.A., Crowther P.A. et al. 2000, *A&A* 353, 624
 Okamoto Y.K., Kataza H., Yamashita T. Miyata T, Onaka T., 2001, *ApJ* 553, 254
 Okamoto Y.K., Kataza H., Yamashita T. et al., 2003, *ApJ*, 584, 368
 Osorio M., Lizano S., D'Alessio P., 1999, *ApJ* 525, 808
 Peeters E., Martin-Hernandez N.L., Damour F., Cox P., Roelfsema P.R. et al. 2002, *A&A* 381, 571
 Price S.D., Egan M.P., Carey S.J., Mizuno D.R., Kuchar T.A., 2001, *AJ*, 121, 2819
 Smith L.J., Norris R.P.F., Crowther P.A., 2002, *MNRAS* 337, 1309
 Stecklum B., Feldt, M. Richichi A. et al. 1997, *ApJ* 479, 339
 Stecklum B., Henning T., Feldt, M. et al. 1998, *AJ* 115, 767
 Stecklum B., Brandl B., Henning T. et al. 2002, *A&A* 392, 1025
 Watson A.M., Hanson M.M., 1997, *ApJ* 490, L165
 Wolfire, M.G., Churchwell, E. 1994, *ApJ*, 427, 889
 Wood D.O.S., Churchwell E., 1989, *ApJS*, 69, 831

This paper has been typeset from a \LaTeX file prepared by the author.

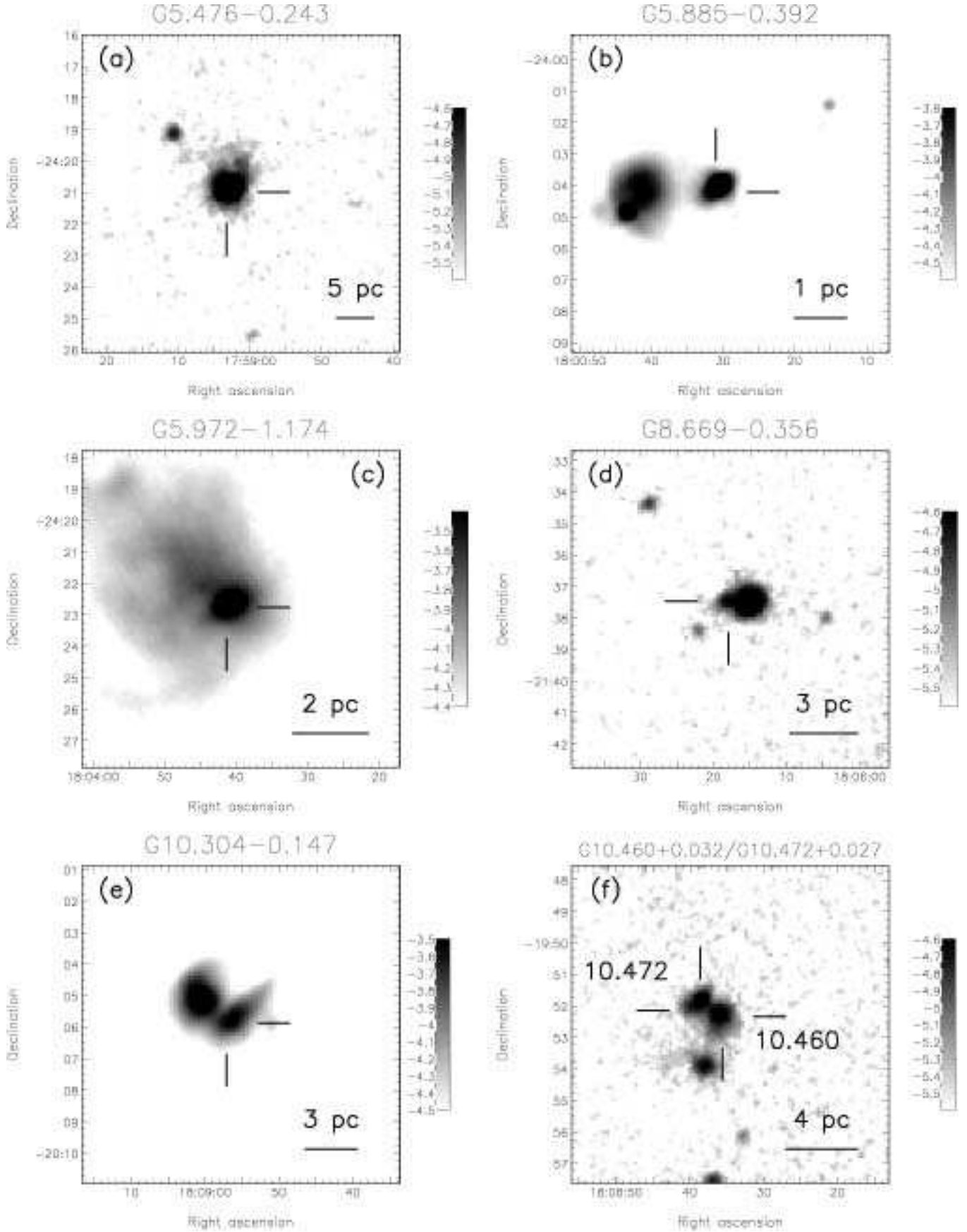


Figure A1. MSX Band E images of UCH II regions. Each field covers a field-of-view of 10×10 arcmin, and is presented in a logarithmic intensity scale (units are $\text{W m}^{-2} \text{sr}^{-1}$)

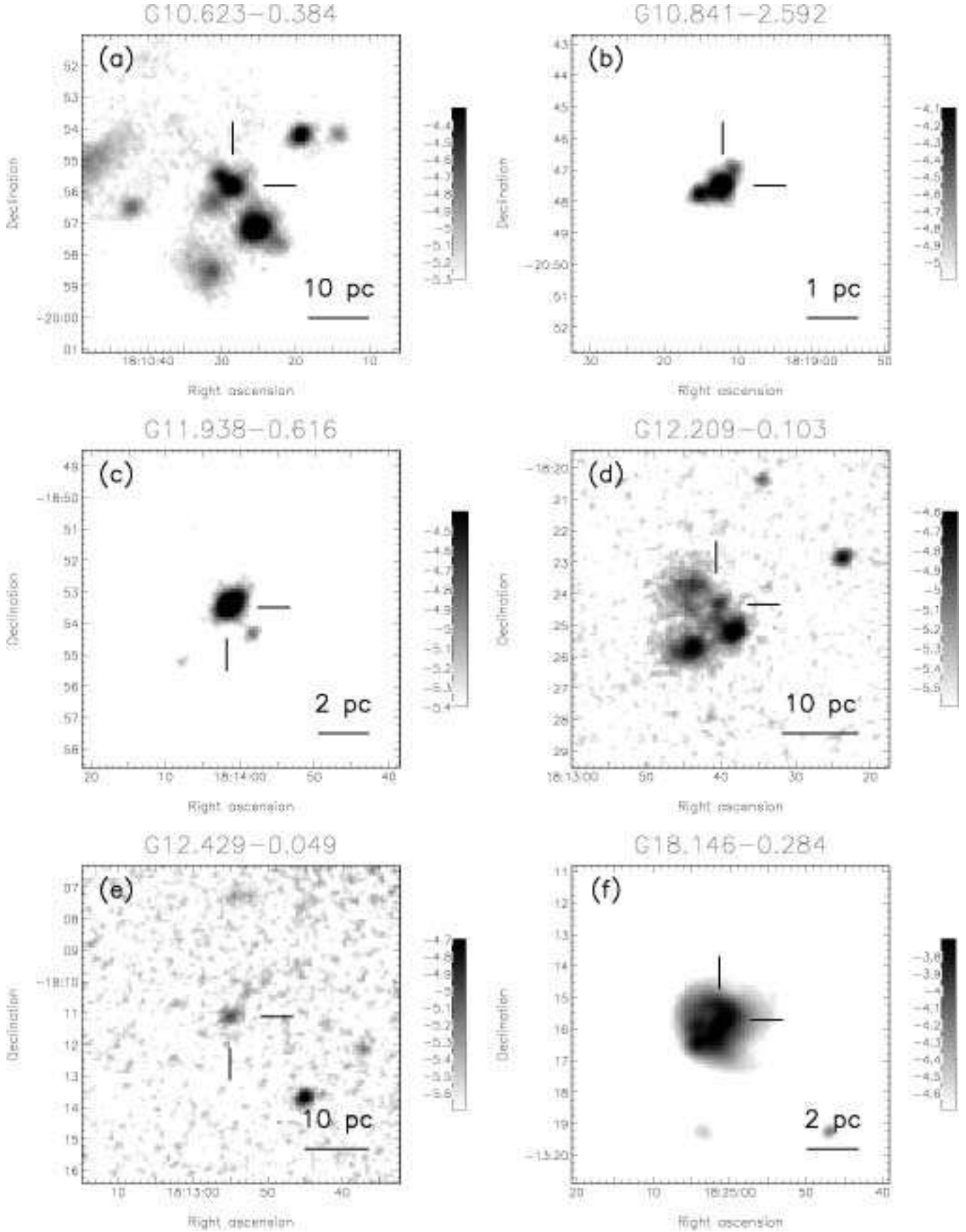


Figure A2: MSX Band E images of UCH II regions. Each field covers a field-of-view of 10×10 arcmin, and is presented in a logarithmic intensity scale (units are $\text{W m}^{-2} \text{sr}^{-1}$)

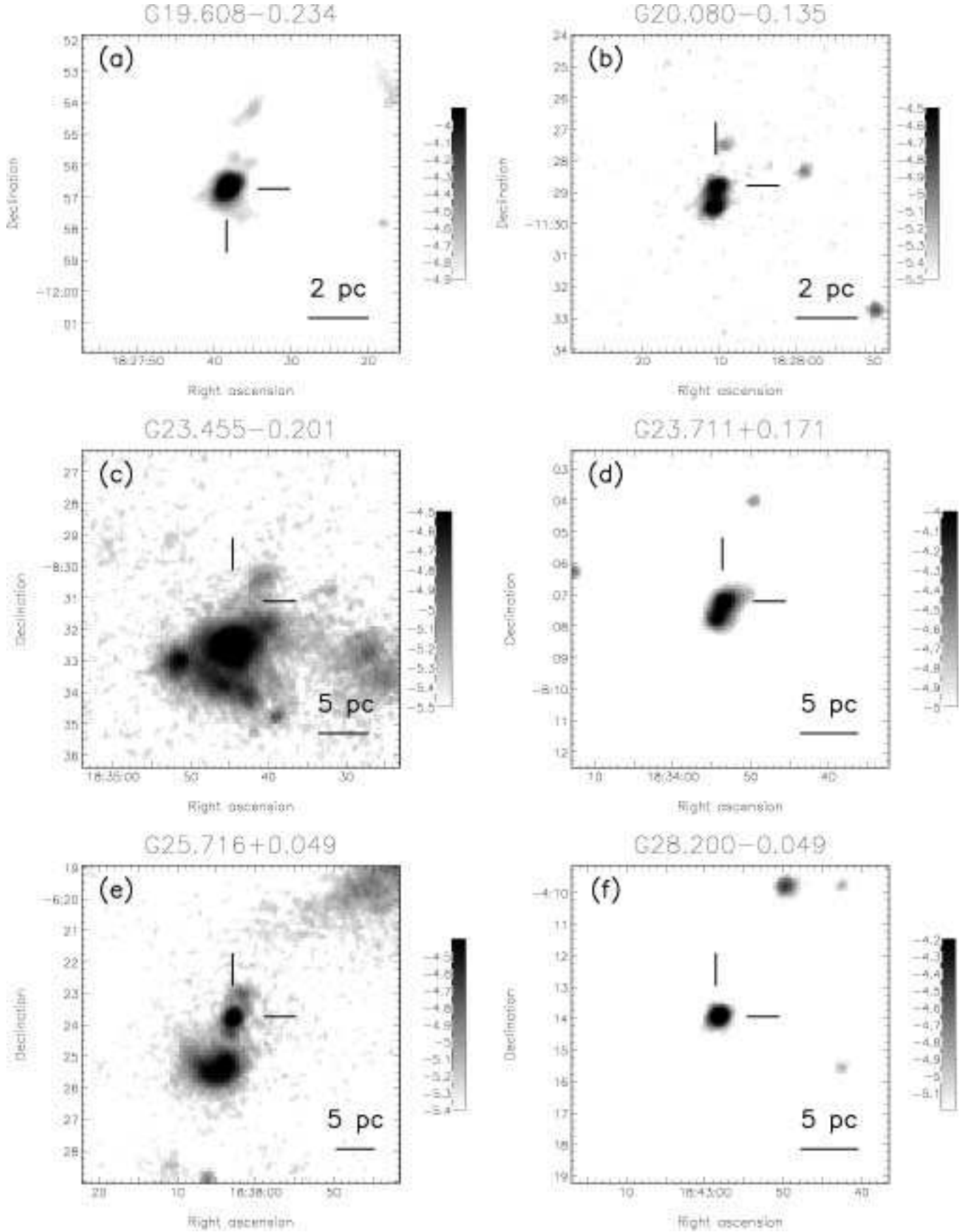


Figure A3: MSX Band E images of UCH II regions. Each field covers a field-of-view of 10×10 arcmin, and is presented in a logarithmic intensity scale (units are $\text{W m}^{-2} \text{sr}^{-1}$)

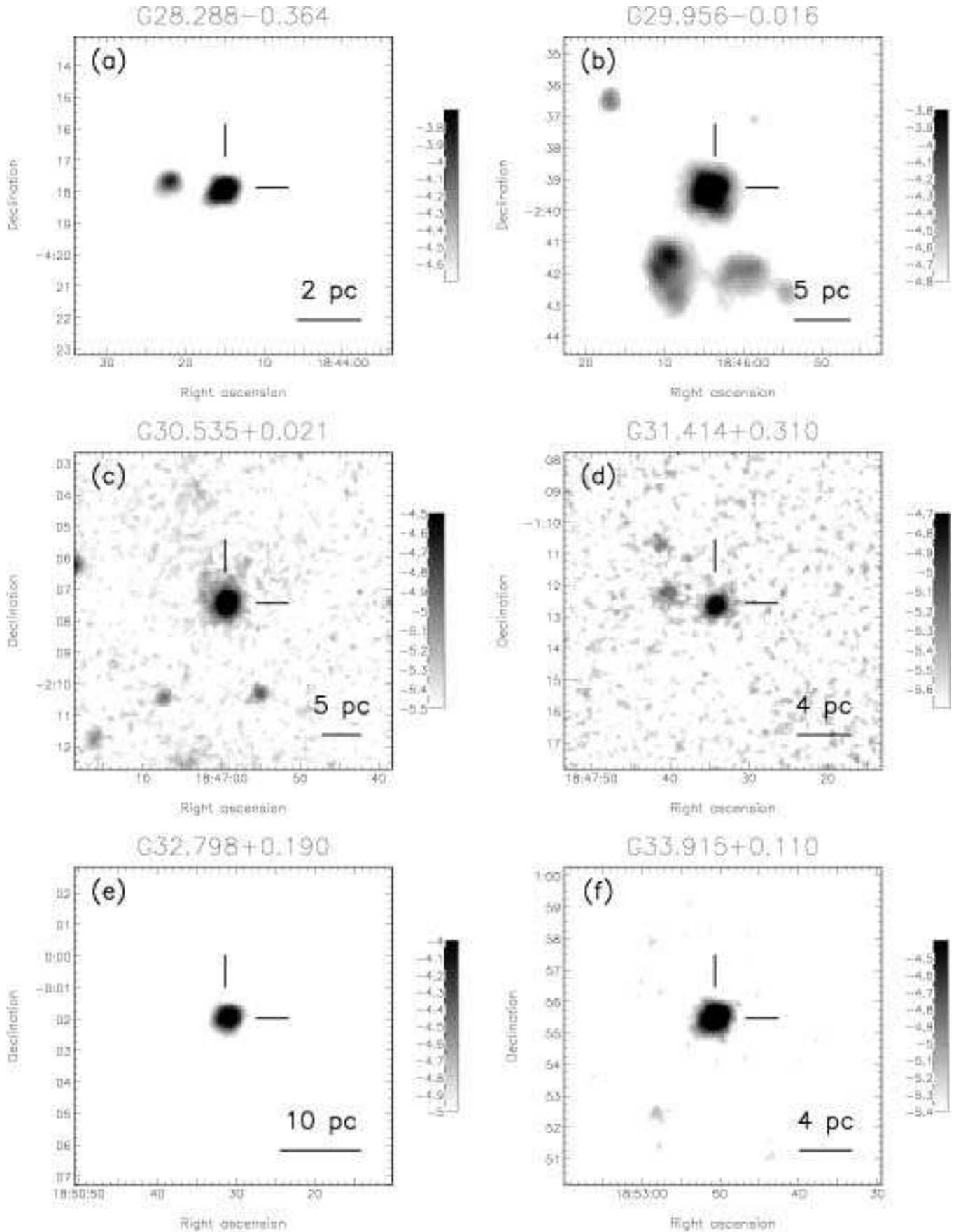


Figure A4: MSX Band E images of UCH II regions. Each field covers a field-of-view of 10×10 arcmin, and is presented in a logarithmic intensity scale (units are $\text{W m}^{-2} \text{sr}^{-1}$)

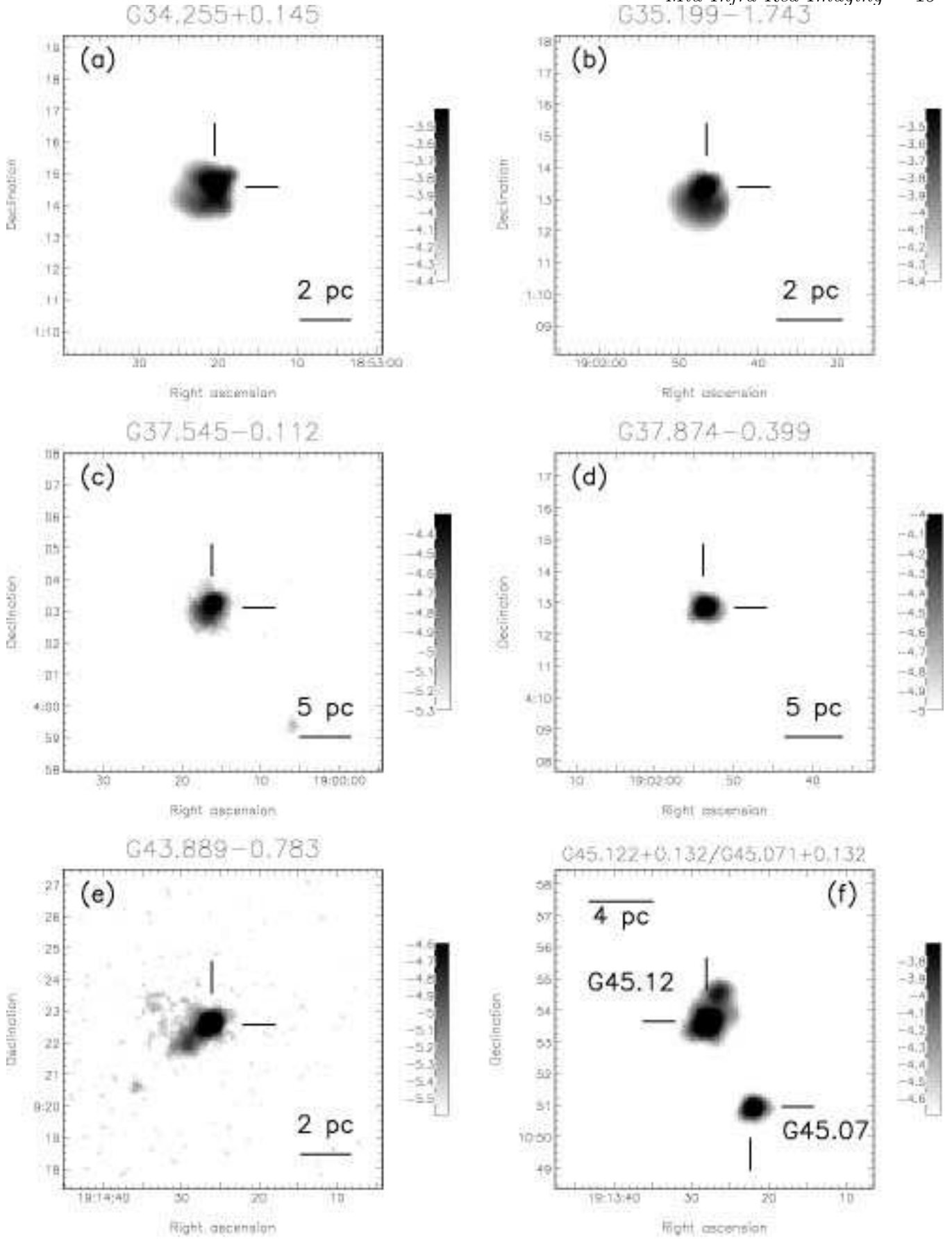


Figure A5: MSX Band E images of UCH II regions. Each field covers a field-of-view of 10×10 arcmin, and is presented in a logarithmic intensity scale (units are $\text{W m}^{-2} \text{sr}^{-1}$)

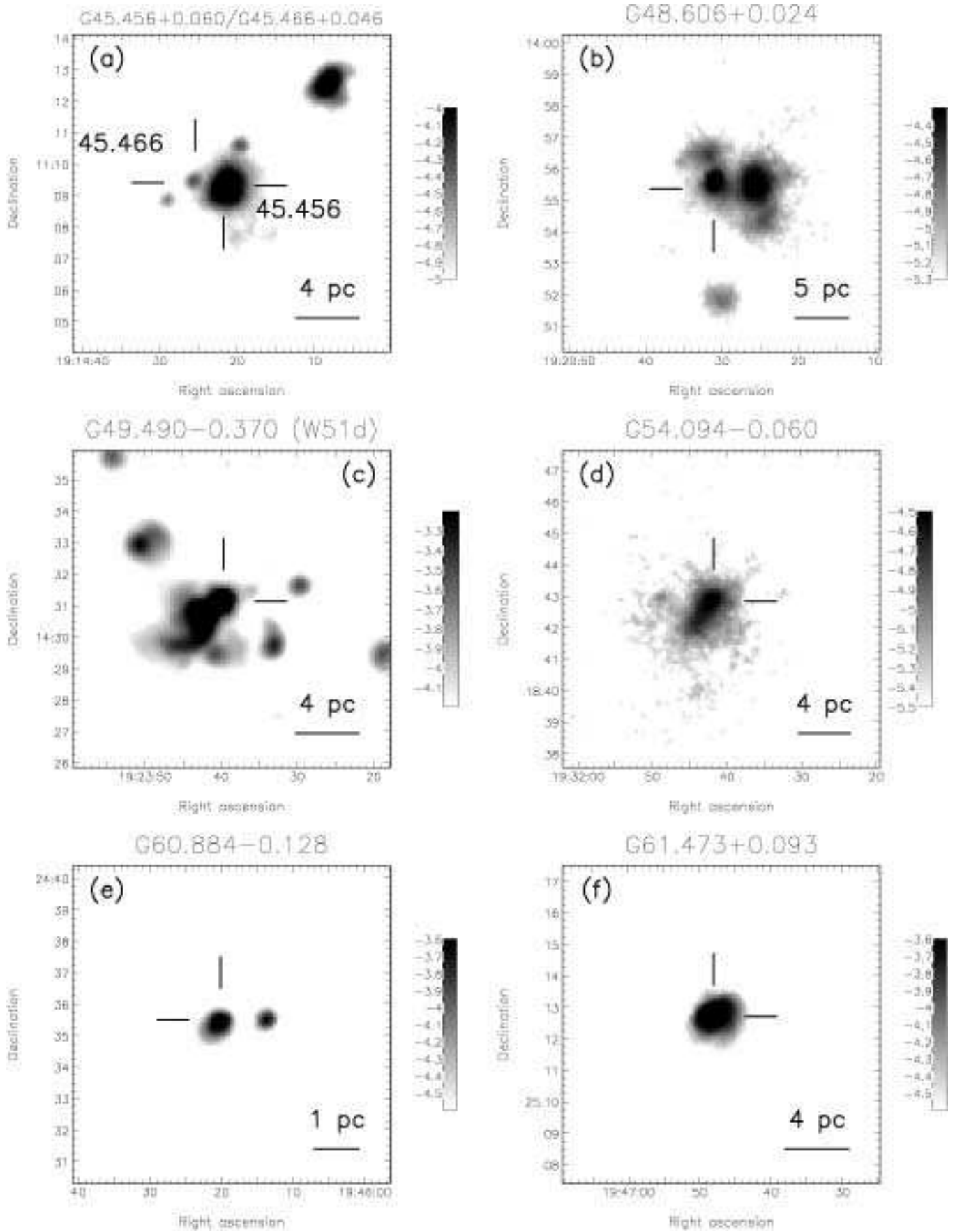


Figure A6: MSX Band E images of UCH II regions. Each field covers a field-of-view of 10×10 arcmin, and is presented in a logarithmic intensity scale (units are $\text{W m}^{-2} \text{sr}^{-1}$)

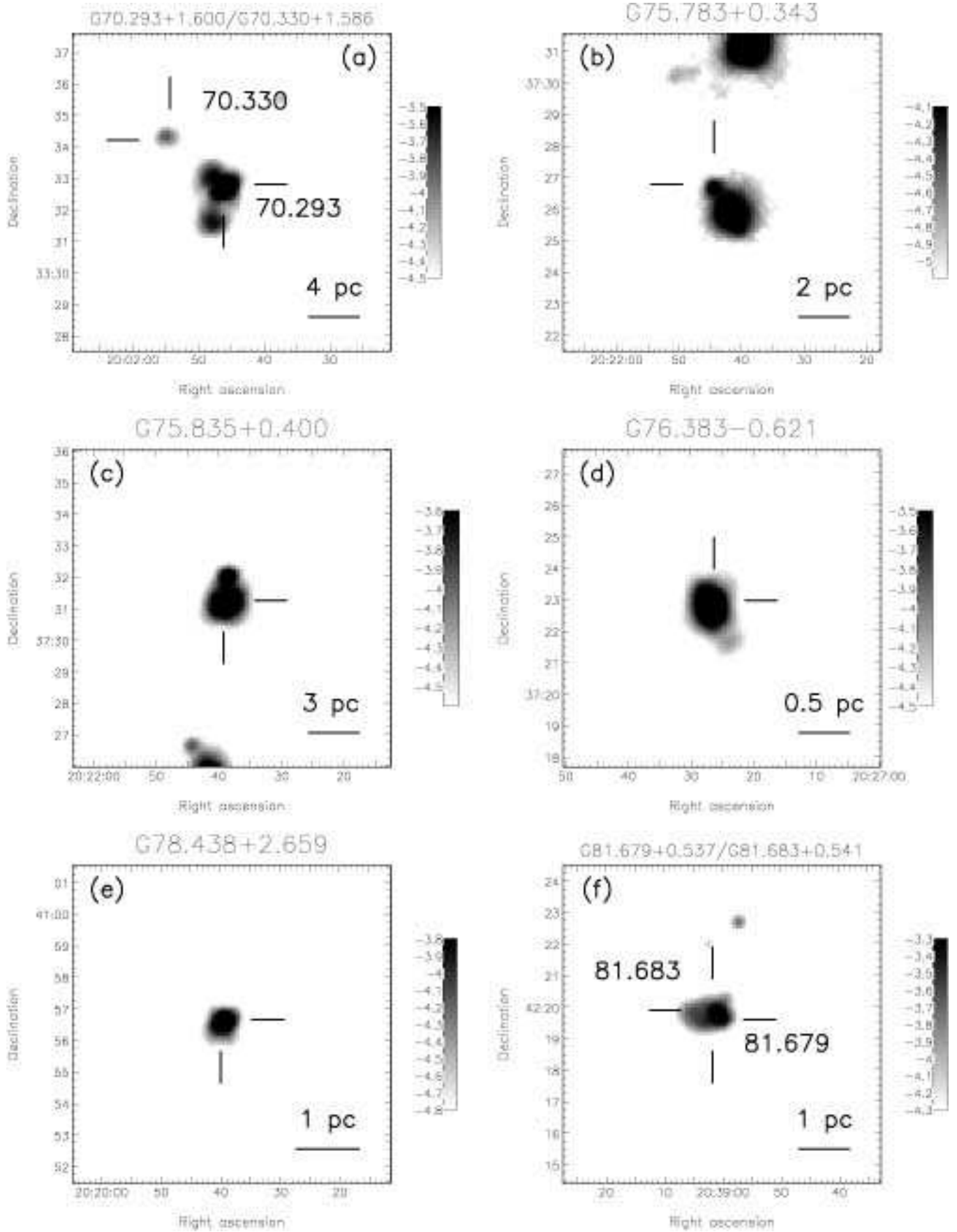


Figure A7: MSX Band E images of UCH II regions. Each field covers a field-of-view of 10×10 arcmin, and is presented in a logarithmic intensity scale (units are $\text{W m}^{-2} \text{sr}^{-1}$)

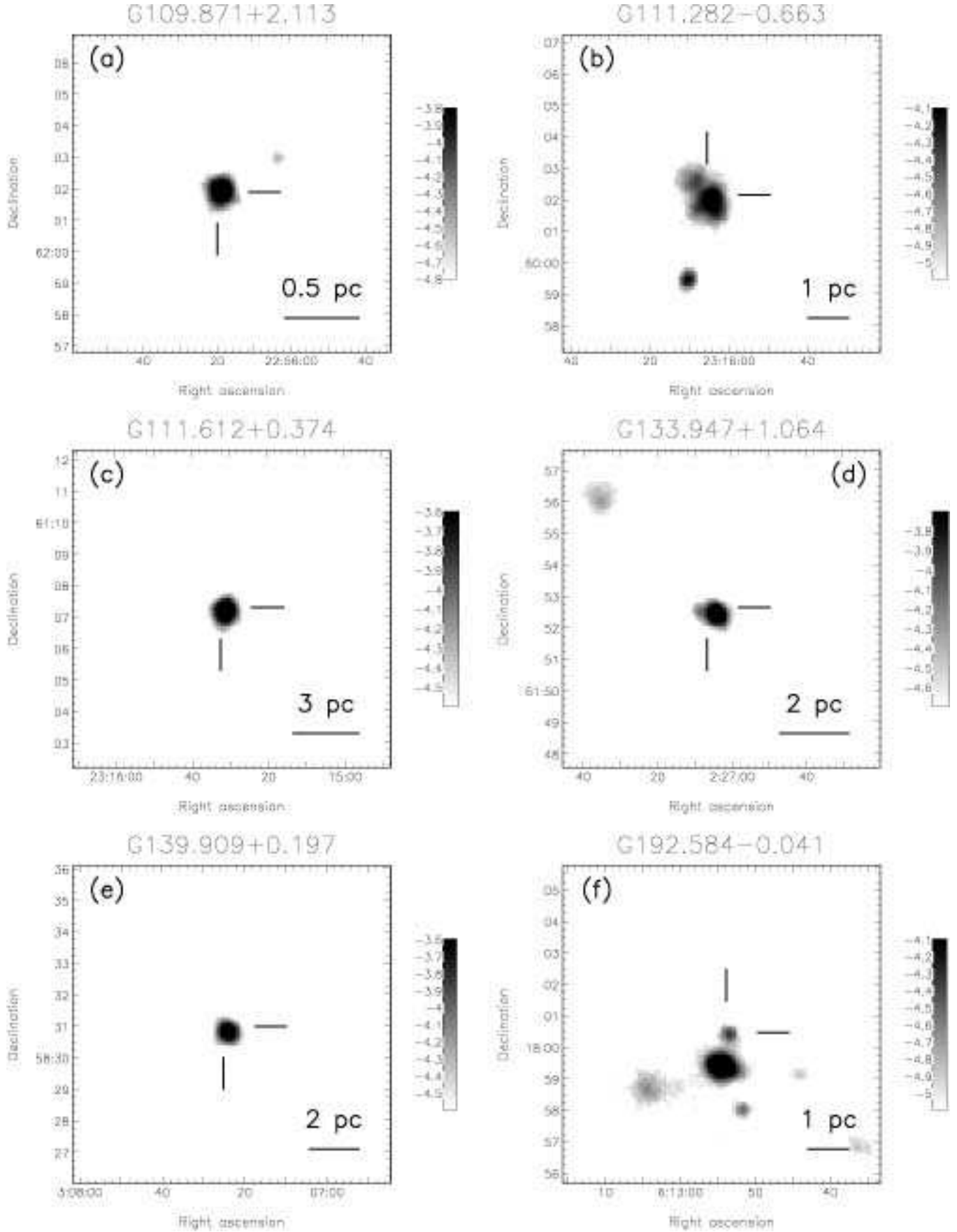


Figure A8: MSX Band E images of UCH II regions. Each field covers a field-of-view of 10x10 arcmin, and is presented in a logarithmic intensity scale (units are $\text{W m}^{-2} \text{sr}^{-1}$)

